2023

Biologically – Plausible Load Feedback from Dynamically Scaled Robotic Model Insect Legs

William Zyhowski
West Virginia University, wz00007@mix.wvu.edu

Biologically – Plausible Load Feedback from Dynamically Scaled Robotic Model Insect Legs

William Zyhowski

Thesis submitted to the
Benjamin N. Statler College of Engineering and Mineral Resources
at West Virginia University
in partial fulfillment of the requirements
for the degree of

Master of Science
In
Mechanical Engineering

Nicholas Szorcinski, Ph.D., Chair
Xi Yu, Ph.D.
Sergiy Yakovenko, Ph.D.
Yong-Lak Park, Ph.D.

Department of Mechanical and Aerospace Engineering

Morgantown, West Virginia
2023

Keywords: campaniform sensilla, dynamic scaling, insects, strain gauges, legged locomotion, robotics

Abstract

Biologically – Plausible Load Feedback from Dynamically Scaled Robotic Model Insect Legs

William Zyhowski

Researchers have been studying the mechanisms underlying animal motor control for many years using computational models and biomimetic robots. Since testing some theories in animals can be challenging, this approach can enable unique contributions to the field. An example of a system that benefits from this modeling and robotics approach is the campaniform sensillum (CS), a kind of sensory organ used to detect the loads exerted on an insect's legs. The CS on the leg are found in groups on high-stress areas of the exoskeleton and have a major influence on the adaptation of walking behavior. The challenge for studying these sensors is recording CS output from freely walking insects, which would show what the sensors detect during behavior. To address this difficulty, 3 dynamically scaled robotic models of the middle leg of the stick insect *Carausius morosus (C. morosus)* and the fly *Drosophila melanogaster (D. melanogaster)* were constructed. Two of the robotic legs model the *C. morosus* and are scaled to a stick insect at a ratio of 15:1 and 25:1. The robotic fly leg is scaled 400:1 to the leg of the *D. melanogaster*. Strain gauges are affixed to locations and orientations that are analogous to those of major CS groups. The legs were attached to a linear guide to simulate weight and they stepped on a treadmill to mimic walking.

Using these robotic models, it is possible to shed light on how the nervous system of insects detects load feedback, examine the effect of different tarsi designs on load feedback, and compare the CS measurement capabilities of different insects. As mentioned earlier, robotic legs allow for any experiment to be conducted, and strain data can still be recorded, unlike animals. I subjected the 15:1 stick leg to a range of stepping conditions, including various static loading, transient loading, and leg slipping. I then processed the strain data through a previously published dynamic computational model of CS discharge. This demonstrated that the CS signal can robustly signal increasing forces at the beginning of the stance phase and decreasing forces at the end of the stance phase or when the foot slips.

The same model leg can then be further expanded upon, allowing us to test how different tarsus designs affect load feedback. To isolate various morphological effects, these tarsi were developed with differing degrees of compliance, passive grip, and biomimetic structure. These experiments demonstrated that the tarsus plays a distinct role in loading the leg because of the various effects each design had on the strain. In the final experiment, two morphologically distinct insects with homologous CS groups were compared. The 400:1 robotic fly middle leg and the 25:1 robotic stick insect middle leg were used for these tests. The measured strains were notably influenced by the leg morphology, stepping kinematics, and sensor locations. Additionally, the sensor locations were lacking in one species in comparison to the other measured strains that were already being measured by the present sensors. These findings contributed to the understanding of load sensing in animal locomotion, effects of tarsal morphology, and sensory organ morphology in motor control.

Table of Contents

List of Tables

List of Figures

Acknowledgments

I want to start by expressing my gratitude to my advisor Dr. Nicholas Szorcinski for their support and guidance over these past few years. Joining the lab has helped me expand my knowledge and skills to heights I could have never imagined.

Additionally, I want to thank the entire NeuroMINT lab. It was through their collaboration that my research was able to be so successful.

I would also like to thank my research committee members Dr. Xi Yu, Dr. Sergiy Yakovenko, and Dr. Young-Lak Park. I could never have finished such a project without their time commitment and breadth of expertise.

Finally, I would like to thank my beloved partner, Jennifer Greenleaf. They have stuck with me through every challenge and helped shape me into a better man. Additionally, they have proofread all my writing, hopefully sparing my professors and colleagues from my unfiltered writing style. I am incredibly grateful for everything they have done and am looking forward to our future together.

1. Introduction

Locomotion is dependent on the capacity to detect and react to dynamic stimuli. Insects have numerous sensory organs that respond to such stimuli. As a result, they serve as useful models for the creation and control of robots. There is a lot of knowledge about how insects control their movement, but many internal aspects of their sensory and neural control systems remain unknown. By creating these bio-inspired robotic models, it may provide insight into the function of an insect's nervous system and sensory networks while also creating robots that utilize these beneficial biological mechanisms.

One commonly studied insect sensor is the campaniform sensillum (CS). CS are mechanoreceptors embedded in the insect's cuticle which encode load (1–3). They are typically located in groups where they experience high stress and undergo microscopic strains when loaded (4,5). CS create dynamic discharge patterns, with many adapting their rate of firing action potentials in response to tonic forces. The ability of CS to encode many aspects of the force exerted on the leg has been demonstrated in recordings from standing and walking animals (6,7). However, it can be difficult to record from multiple CS groups at once.

To record strain from all sensors in the leg as it steps, 3 dynamically scaled robotic legs based on model insects *Carausius morosus* (*C. morosus)* and *Drosophila melanogaster (D. melanogaster)* that incorporate sense organs were developed. Two of the robotic legs are based on the *C. morosus* which have a ratio of 15:1 (Figure 1) and 25:1 compared to the stick insect. In comparison to the fly, the robotic *D. melanogaster* leg is scaled 400:1. The robotic stick leg (15:1) underwent biological experiments, different types of leg loading, and foot slipping. This data was then run through a mathematical model of how the receptor converts strains into neural activity (8). The robotic model was further expanded upon with the addition of various tarsi styles that

have different degrees of compliance, passive grip, and biomimetic structure. The robotic model also allowed us to compare homologous CS groups using the 25:1 stick leg and the 400:1 fly leg, even though these species are noticeably different. Using this information, I propose theories about the role of sensory organ morphology, tarsal morphology, and load sensing in animal locomotion and motor control. Chapter 2 presents background on the function of CS and prior work modeling them. Chapter 3 outlines the methodology for the design and implementation of each robotic leg model. Chapter 4 details the verification of the robotic leg model utilizing the 15:1 robotic stick leg to encode forces in various biological experiments. Chapter 5 expands upon the 15:1 robotic stick leg with the addition of tarsi with differing degrees of compliance, passive grip, and biomimetic structure. Chapter 6 explores the comparison of strain changes that occurred during stepping in the 25:1 stick and 400:1 fly robotic legs. Chapter 7 is the discussion and chapter 8 is the conclusion.

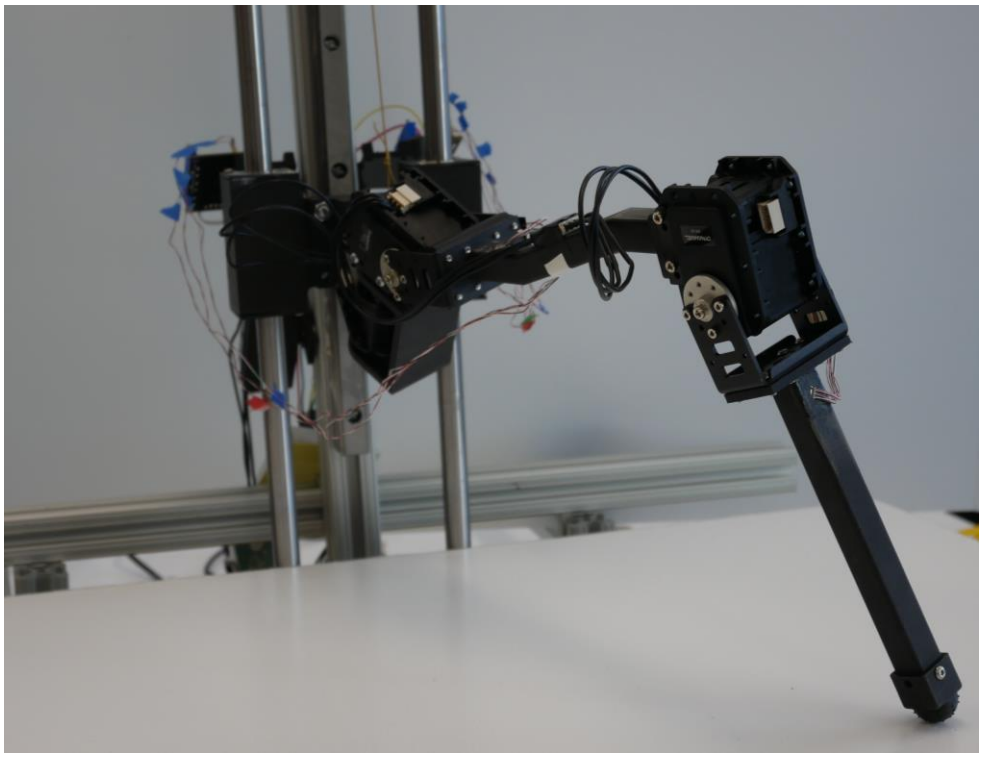

Figure 1: Dynamically scaled *C. morosus* robotic leg attached to linear guide

2. Background

2.1 Campaniform Sensilla (CS)

Animal legs experience a range of forces during walking. Generally modest forces are produced by the muscles during the swing phase. During the stance phase, much stronger forces are generated when the legs contact the ground. In insects, CS receptors measure the strain on the exoskeleton to detect forces (1,3,9). The CS operates by generating action potentials when cuticular deformations compress a CS which makes the collar indent the cuticular cap. This compresses the dendrite causing its mechanotransduction channels to open. (2). Figure 2 depicts a schematic of a CS cap.

Numerous clusters or groups of CS are found on the exoskeleton near high stress areas of the leg. Due to their oval shape, most CS are directionally sensitive. They respond best to compression along the short axis (1). This implies that depending on how they are oriented within the cuticle, even adjacent CS may have varying sensitivities to strain (9,10). Additionally, CS can be round which makes them sensitive in all directions, or exhibit directional sensitivity if the cap and surrounding collar are asymmetrically coupled (11). These various axis orientations create functional subunits within each field because of similar short-axis orientations of multiple sensors (10). Groups 3 and 4, for instance, are perpendicular to one another and are located on the dorsal side of the stick insect trochanter (Figure 3A). This enables these groups to measure the strain on the leg as it bends downward (group 4) and upward (group 3).

According to earlier research, CS discharges in walking happen almost exclusively when muscles contract against resistance during the stance phase. CS then function as proprioceptive sense organs monitoring the animal's behaviors by detecting the net effect of resisted muscle

forces and variation in leg load (12). When an insect is walking, these signals are used to modify the timing of phase transitions and strength of muscle contractions (13,14).

Since the net rotational forces are about the joint and independent of joint angles, it is possible to calculate the strains in the exoskeleton at the locations as a function of joint torques (15). Recent research has concentrated on the signals produced by the tibial group of CS joint torques calculated by inverse dynamics. These torque timecourses were obtained from stick insects that were allowed to freely move across flat or sloping surfaces (16–19). These studies have demonstrated the dynamic sensitivities of the receptors, which enable them to precisely monitor variation in forces (16–19). The rate of change of forces, which previous studies have referred to as “yank”, dominates the sensory discharge (20). The ongoing variation of the muscle contractions that produce the gradual, smooth movements that distinguish animal walking behavior from that of many robots may depend on these sensitivities (21).

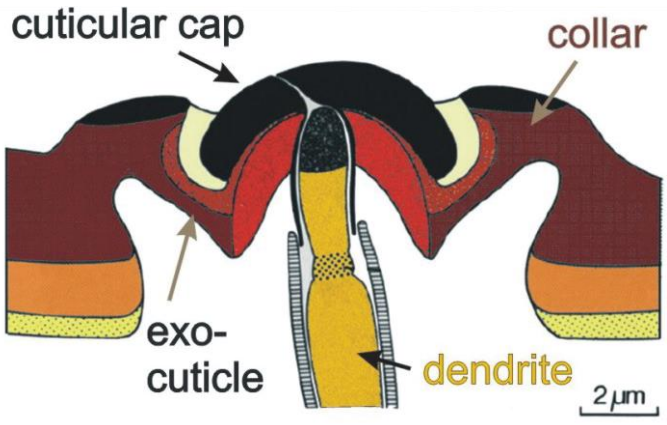

Figure 2: Diagram of Campanifor Sensilla from Grünert et al. 1987 **(22)**

The *C. morosus* has four fields of CS on its anterior, dorsal, and posterior faces that are used to encode external loads and strains (9,10). G1 and G2 on the posterior and anterior trochanters, respectively (Figure 3A), monitor load in the posterior and anterior direction, according to electrophysiological studies conducted on *C. morosus* (10,23,24). The dorsal

trochanter's G3 encodes increases in dorsal load and decreases in ventral load (9), while the dorsal trochanter's G4 mirrors these signals (9). The load variations in the dorsal-ventral plane of the coxa-trochanter joint are encoded by G3 and G4 together (9).

Although morphologically different, other insects, such as the fruit fly *D. melanogaster* (Figure 3B), have CS in some of the same leg locations, suggesting potential functional homology (4,25,26). The two subunits that make up the trochanter field (TrF), which is homologous to G3 and G4, are located on the *D. melanogaster* trochanter. (25,27,28). Additionally, three sensors with identical axis orientations are present in a group on the posterior trochanter. The anterior trochanteral CS is present in the *C. morosus* but absent in the *D. melanogaster* (4).

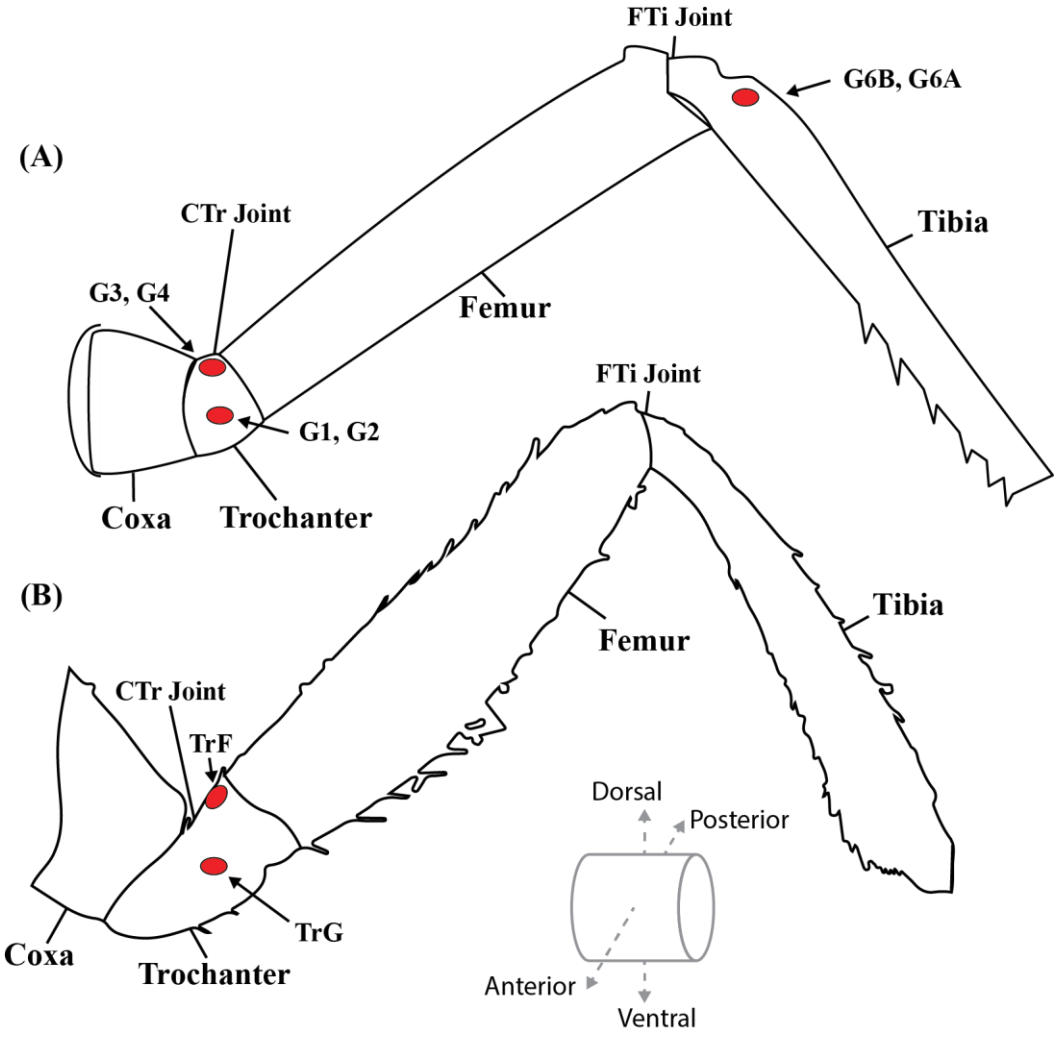

Figure 3: (A) Diagram of CS locations on stick insect leg modified from image courtesy of Dr. Sasha Zill (Anterior view). Groups 3,4, 6B, and 6A are marked. Leg components and joints are labeled except the ThC joint is absent on this diagram. (B) Diagram of CS locations on fly leg based on Dinges et al. 2022 (Anterior view) **(29)**. TrF and TrG groups are marked. Leg components and joints are labeled except the ThC joint is absent on this diagram

2.2 Bio-inspired Robot Models

For years, researchers have used biomimetic robots and computational models to learn more about the processes that underlie animal motor control (30). Why build a physical robot to study motor control instead of a computer simulation? Robotic models of animals must confront the full physics of the environment being modeled which can complement purely computational models. Currently, multi-body physics simulators almost always model leg segments as "rigid bodies" that cannot bend, which makes it difficult to measure the minute strain of the leg segments as the leg moves. Insights into how insects detect strain have been gained by using computational modeling techniques like Finite Element Analysis (FEA) to predict how complex shapes like insect leg segments would deform under stress (29,31–34). A difficult problem that a robotic model inherently solves is finding and applying a realistic stress profile to the model. Additional factors that affect the load on each leg segment include ground contact forces such as static and sliding friction are notoriously difficult to model (35,36).

The ability to use robotic representations of animal legs to create walking robots that directly apply biological principles to locomotion is another benefit of such models. A neuromechanical model of insect walking (37) was used to create the SCASM (Sensory Coupled Action Switching Modules) single-leg stepping controller (38) that was later incorporated into Bill-Ant (39) to investigate how load feedback affected the coordination of the joints throughout one leg. The robot Octavio (40) was created using the same neuromechanical model, and its one leg and entire body were tested using biologically based control networks (40,41). The full

dynamics of a walking animal were simplified in both of these one-legged robotic models. However, with each single-leg model, the researchers were able to test in depth how the design and fine-tuning of the control system produced reliable stepping without the additional challenges brought on by the presence of additional legs. Furthermore, once the other legs were included, their findings appeared to be sufficiently generalizable to be applied to leg control. The use of single leg robotic models (like those in my work) to comprehend the control of walking in both animals and robots is supported by advancements like these.

In order to mimic CS, several contemporary robots, such as Hector (42), Mantisbot (43), and Drosophibot (44), have utilized strain gauges. These robots were created as bio-inspired replicas of three different insects: the stick insect, praying mantis, and fruit fly, respectively. To the authors' knowledge, only Drosophibot's strain gauge feedback filter can mimic the dynamics of CS, and this function has only been put to the test in simulation.

3. Methodology

3.1 Robotic Legs Construction

Three Dynamixel servomotors (MX-28), Dynamixel brackets, and 3D-printed parts make up each of the three robotic legs in Figure 4. The servomotors are connected in series to apply balanced loads to each servomotor shaft. This is crucial because it enables the strain to concentrate at CS sites just as it does in the animal. The robotic legs are constructed to have the same segmental proportions as the middle leg of a *C. morosus* and *D. melanogaster*, the legs are 15:1, 25:1, and 400:1 scale models respectively (12,45–47). Table 1 lists these ratios. Each leg segment is constructed of hollow square tubes. The tubes were produced using a Markforged Mark II 3D printer (48) and the material Onyx (49). Hollow tubes are used in the construction process because the insect exoskeleton can be approximated as hollow tubes (50).

Table 1: Comparison of *C. morosus* and *D. melanogaster* leg segment to that of the robotic *C. morosus* and *D. melanogaster* leg (mm). The *C. morosus* leg segment lengths are from Table 1 of Theunissen et al. 2015 **(46)**.

Middle Leg Segments (mm)			
	coxa	femur	tibia
C. morosus	1.42	11.6	11.2
D. melanogaster	0.07	0.71	0.70
Stick Robotic Leg (15:1)	21	171.50	165.60
Stick Robotic Leg (25:1)	34.5	284	274
Fly Robotic Leg (400:1)	28	284	280

The thorax-coxa (ThC), coxa-trochanter (CTr), and femur-tibia (FTi) joints are marked on the legs in Figure 5. The ThC servomotors are attached to a carriage that can freely move along a linear guide with a vertical orientation. The carriage mimics the mass and motion of an insect's body. The strain data is captured by strain gauge rosettes. The rosettes' positions and orientations are analogous to those of the major CS groups on the fly and stick insect (51–53). A more detailed

description of the locations and orientations of the CS on the fly and stick robotic legs can be found in Gesa et al. 2023 (47).

Figure 4: Robotic Leg Pictures. (A) *C. morosus* 15:1 scaled leg, (B) *C. morosus* 25:1 scaled leg, (C) *D. melanogaster* 400:1 scaled leg

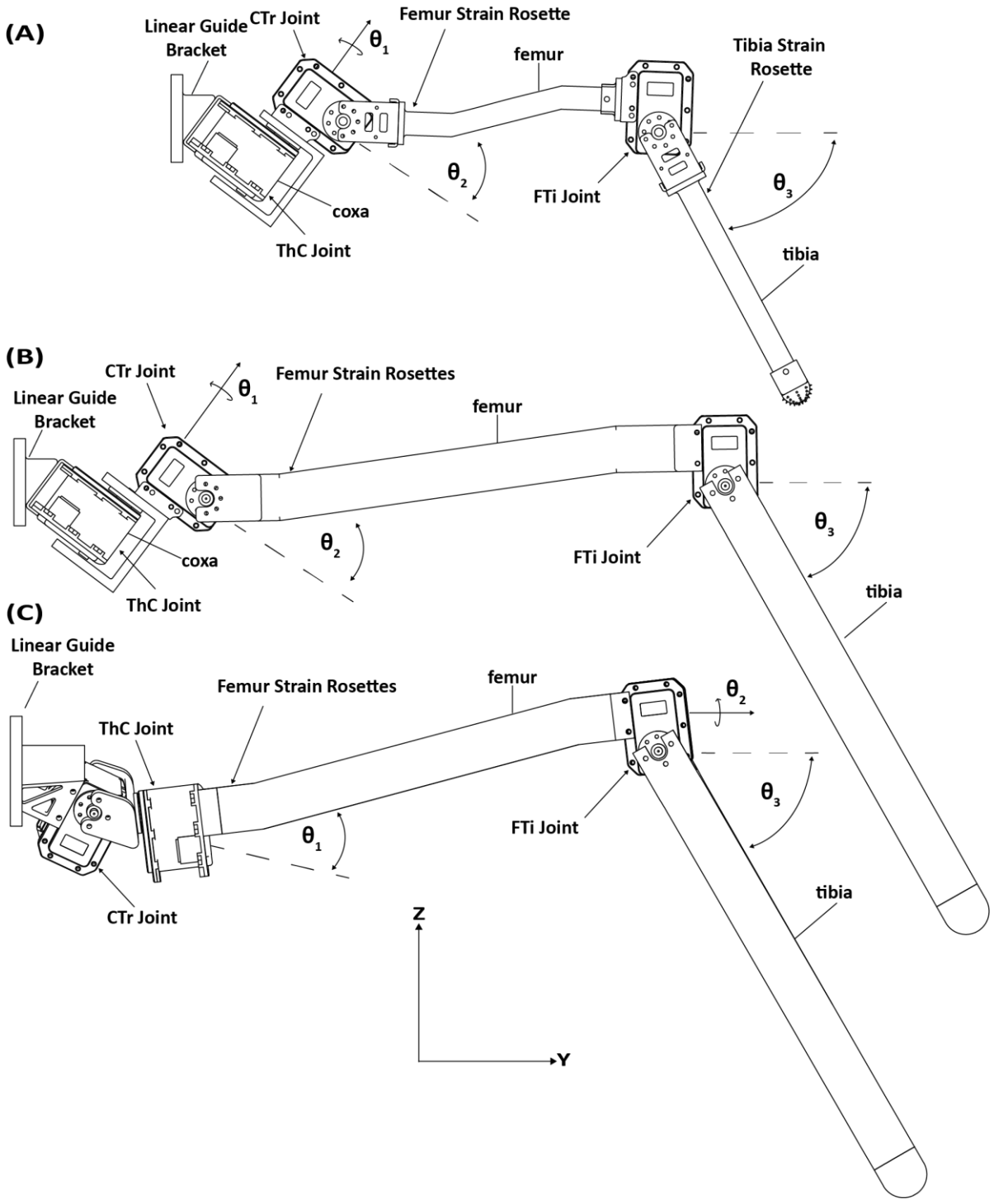

Figure 5: Robotic middle legs with three degrees of freedom. The leg segments, joint axes, and joint angles are indicated. (A) *C. morosus* 15:1 scaled leg, (B) *C. morosus* 25:1 scaled leg, (C) *D. melanogaster* 400:1 scaled leg

3.2 Robot Kinematics

The legs were created to have the same ranges of motion as the middle leg of the *C. morosus* and *D. melanogaster* (45,46,54,55). A series of homogenous transformation matrices that are linked together using the product of exponentials formula shown in equation **(1)** can be used to represent the forward kinematics of the legs (56). The angle of the ThC joint in the legs is θ_1, the angle of the CTr joint is θ_2, and the angle of the FTi joint is θ_3 (56):

$$\boldsymbol{g_d(\theta_1, \theta_2, \theta_3) = e^{\hat{\xi}_1 \theta_1} e^{\hat{\xi}_2 \theta_2} e^{\hat{\xi}_3 \theta_3} g_{st}} \quad \textbf{(1)}$$

The configuration of the foot in relation to the body is described by the 4x4 matrix g_d, which is expanded in equation **(2)**. The foot is rotated in space according to the upper-left 3x3 block of the matrix, R. The foot is positioned in space according to the upper-right 3x1 vector, p. The lower-left 1x3 vector is 0, and the lower-right element is 1:

$$\boldsymbol{g_d(\theta_1, \theta_2, \theta_3) = \begin{bmatrix} R(\theta_1, \theta_2, \theta_3) & p(\theta_1, \theta_2, \theta_3) \\ 0 & 1 \end{bmatrix}} \quad \textbf{(2)}$$

Each matrix exponential $e^{\hat{\xi}_i \theta_i}$ in equation **(3)** is built in the same configuration, but with joint-specific twists, ξ_i, constructed from the information in Table 2. The upper-left 3x3 rotation matrix R is constructed using Rodrigues' rotation formula (equation **(4)**) and the upper right 3x1 translation matrix p is calculated from components of the twist (equation **(5)**). In those formulas *I* is the identity matrix, Ω_i is a skew matrix of ω_i, and v_i (equation **(6)**) is the linear velocity. The g_{st} matrix represents the end effector in zero configuration, which defines when the three joint angles are equal to 0. To position the foot in 3D space, the angles θ_1, θ_2, and θ_3 must be calculated utilizing inverse kinematics. In this inverse kinematics problem, 3 joint angles to position the foot in a specific 3D point must be calculated; each foot position has a unique set of joint angles. This means that after establishing a footpath, the joint angles could be uniquely specified. To find the

values of θ_1, θ_2, and θ_3 that satisfy $\vec{f} = \vec{0}$, I first defined the function $\vec{f}$ in equation **(7)** and then used a quasi-Newton method integrated into fsolve of MATLAB (57).

$$e^{\hat{\xi}_i \theta_i} = \begin{bmatrix} \boldsymbol{R(\theta_i)} & \boldsymbol{p(\theta_i)} \\ \mathbf{0} & \mathbf{1} \end{bmatrix} \quad \textbf{(3)}$$

$$\boldsymbol{R(\theta_i) = I + \Omega_i(sin\theta_i) + \Omega_i^2(1 - cos\theta_i)} \quad \textbf{(4)}$$

$$\boldsymbol{p(\theta_i) = \big(I - R(\theta_i)\big)(\omega_i \times v_i) + \omega_i \omega_i^T v_i \theta_i} \quad \textbf{(5)}$$

$$\boldsymbol{v_i = -\omega_i \times q_i} \quad \textbf{(6)}$$

Table 2: Zero configuration vectors. The direction of the twist unit vector is indicated with $\boldsymbol{\omega}$, point on the axis of rotation is indicated with q. (mm)

Zero Configuration Vector									
Stick Leg (15:1)				Stick Leg (25:1)			Fly Leg (300:1)		
	x	y	z	x	y	z	x	y	z
ω_1	0	$-\sin(37°)$	$-\cos(37°)$	0	$-\sin(37°)$	$-\cos(37°)$	cos (20.1)	cos (88.68)	cos (69.96)
ω_2	1	0	0	1	0	0	$-$sin (1.4)	$-$cos (1.4)	0
ω_3	1	0	0	1	0	0	cos (1.4)	sin (1.4)	0
q_1	0	63.46	15.03	0	50	0	0	45.23	15.78
q_2	0	91.39	22.36	0	105.05	14.87	-4.56	67.26	4.26
q_3	0	230.45	-80.90	0	333.04	-154.43	-11.27	355.31	4.28
q_{end}	0	362.42	-180.99	0	500.46	-319.80	-18.12	632.87	4.31

$$\vec{\boldsymbol{f}}(\boldsymbol{\theta_1, \theta_2, \theta_3}) = \vec{\boldsymbol{p}}(\boldsymbol{\theta_1, \theta_2, \theta_3}) - [\boldsymbol{x_{desired}, y_{desired}, z_{desired}}]^T = \vec{\mathbf{0}} \quad \textbf{(7)}$$

The footpaths depicted in Figure 6 were created based on the footpaths of the *C. morosus* and *D. melanogaster* (45). This was accomplished with piecewise polynomials to generate the desired trajectory. When the robot's tarsus was lowered to the treadmill, care was taken to ensure that the tarsus' velocity matched that of the treadmill. This required the tarsus to overshoot the location of the touchdown at the end of the swing, accelerate rearward until its speed matched the treadmill, and then lower to contact the treadmill. Failure to match the tarsus and treadmill speed resulted in "bouncing" of the leg at the start of stance, which is not seen in walking insects (54).

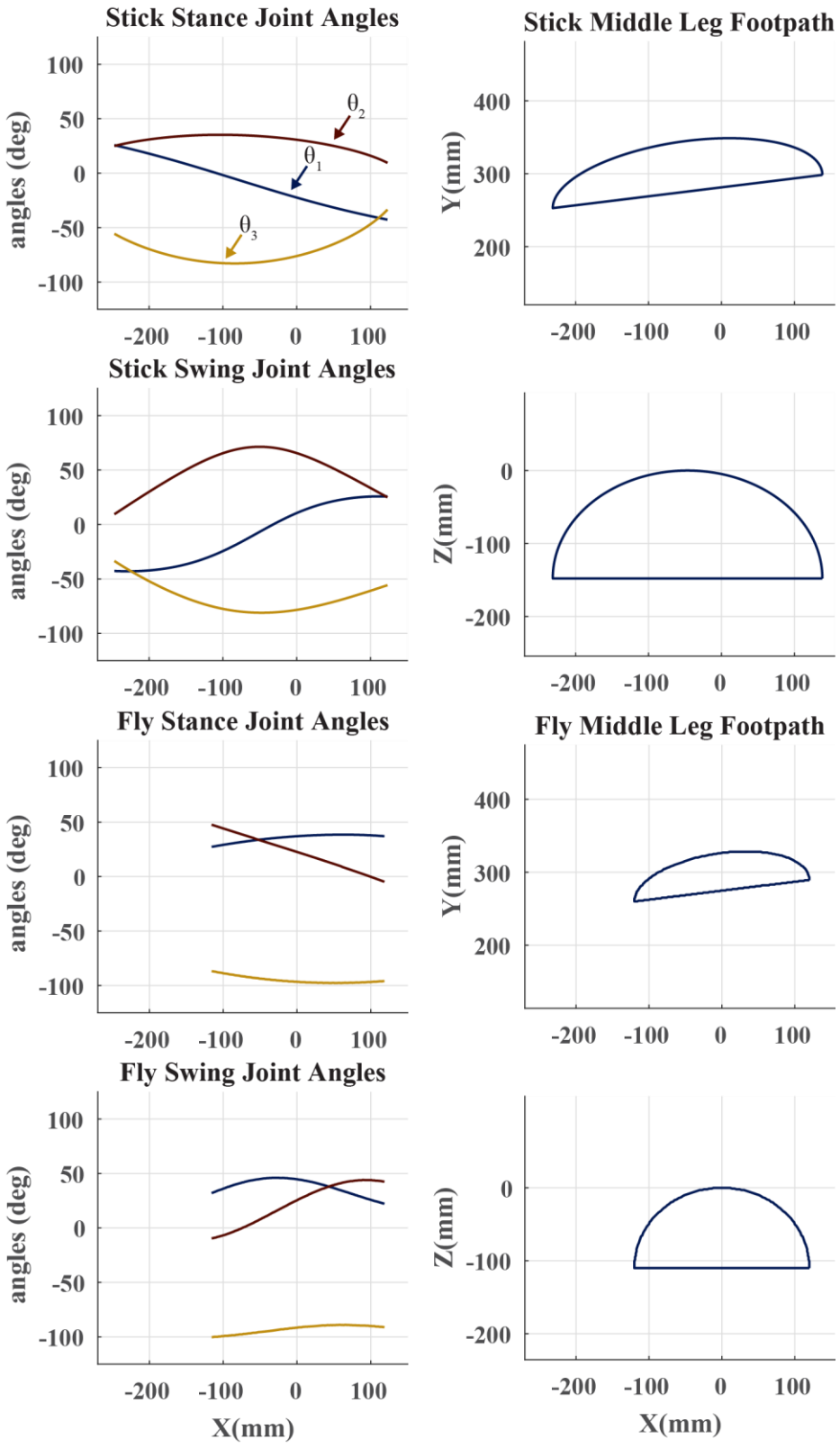

Figure 6: Servomotor angles and footpath for stick and fly robotic legs

3.3 Robotic Control

To control the servomotors, a desktop computer was used to run the MATLAB script. Inverse kinematics was used to determine the servomotor angles from the desired footpath in Figure 6. The angles were then transferred via serial communication to an OpenCM 9.04 microcontroller, that transferred them to the MX 28 dynamixel servomotors. A 60 Hz sample rate was used on the serial bus. The OpenCM also collected the analog strain data and returned it to the MATLAB script. The 12-bit onboard analog to digital converter (ADC) of the OpenCM was used to achieve this. An illustration of this control structure is in Figure 7.

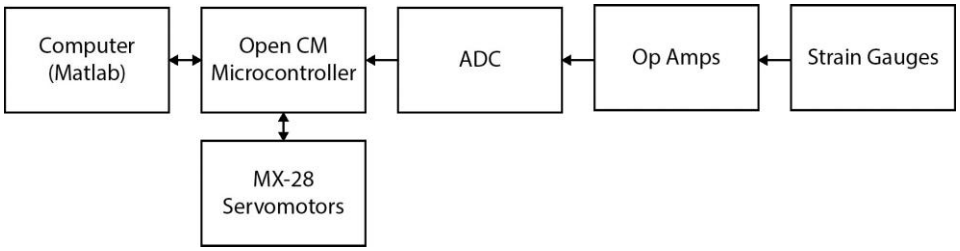

Figure 7: Control structure of robotic legs

3.4 Treadmill and Linear Guide

To enable movements that simulate the leg pushing the body forward, a variable speed treadmill was used. A linear guide was also utilized so that during the stance phase, the linear guide forces the leg to support itself and the guide's weight. A calibrated tachometer is used to synchronize the treadmill with the leg actuators. An illustration of one of the legs (15:1 stick insect) attached to the linear guide and the treadmill it walks on is shown in Figure 8. The same configuration was used for each leg.

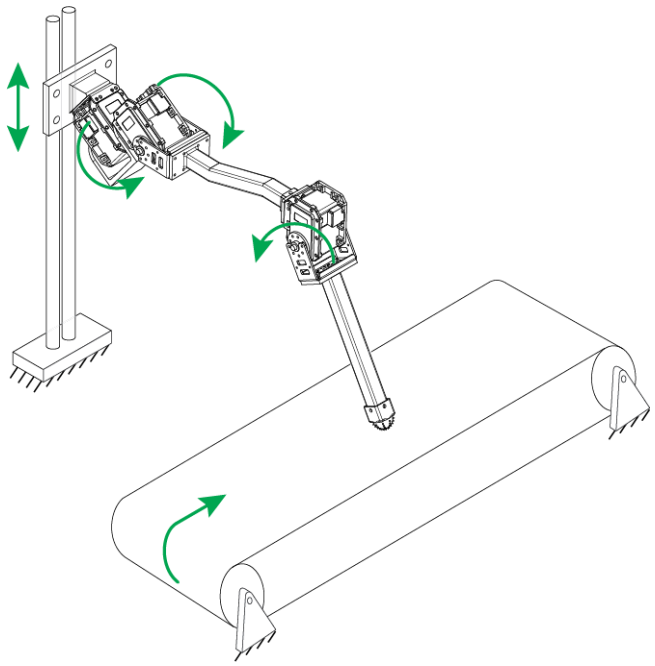

Figure 8: Diagram of leg setup and treadmill. Green arrows denote the type and direction of movement.

3.5 Dynamic Scaling

It is necessary to dynamically scale the robot to the insect. Thus, the inertial, viscous, elastic, and gravitational forces acting on it are balanced in the same way as in the animal of interest (58). The actuation frequency must be the same proportion of the natural frequency of the leg oscillation in both animals and robots to achieve this. This ensures that the robot experiences scaled forces that are similar to what the insect would experience. I therefore estimate the animal's femur-tibia joint natural frequency, compare it to the animal's stepping period, and use the natural frequency of the robotic leg's femur-tibia joint to choose a suitable stepping period for the robot.

The insect's leg is roughly a slender rod with a mass of 11 mg (45) and length of 1.2 cm, meaning its moment of inertia about its end is approximately $J_O = \frac{1}{3} \cdot mL^2 = 5.3 \times 10^{-10}\ kg \cdot m^2$. The passive elastic forces of its muscles determine the stiffness of its femur tibia joint which is about $k_T = 10^{-6} \frac{Nm}{rad}$ (59). Consequently, the femur-tibia joint's natural period is approximately

$T_n = 2\pi/\sqrt{k_T/J_O} = 0.14\ s$. A stick insect's step lasts about 1 second (45), which means that each step is roughly six times longer than the natural period. As a result, the robot's step period should be six times longer than its natural period. The servomotor's rotor is the primary source of inertia for the femur-tibia joint which is equal to about $J_O = 10^{-2}\ kg \cdot m^2$. The feedback controller for the servomotor results in a stiffness of roughly $k_T = 1\frac{Nm}{rad}$. The femur-tibia joint's natural period of oscillation as a result is approximately $T_n = 2\pi\sqrt{k_T/J_O} = 0.63\ s$, and 6 times this value is approximately 4 s. This makes the dynamically scaled step period for the robotic leg 4 s. Using the same procedure, the robotic *D. melanogaster's* step time was determined to be 4 s as well (55,60).

3.6 Strain Gauges

Strain gauges transduce strain as a change in resistance. If coupled with a Wheatstone bridge, when the gauge is disturbed, a slight voltage drop is created across bridge. The OpenCM's ADC and the majority of ADCs are unable to read such tiny voltages. To resolve this issue the signal was amplified using a differential operational amplifier (Op-Amp) in conjunction with two unity buffers to achieve a designated gain of 250, which is a sufficient gain for the ADC to operate. The Op-Amp and Wheatstone bridge which is configured in a quarter bridge is all on one printed circuit board (PCB) whose circuit is in Figure 9. To change the bridge's offset, it has a manually adjustable trimmer potentiometer. Three of these circuits were present on each PCB, enabling the connection of up to three strain gauges per board.

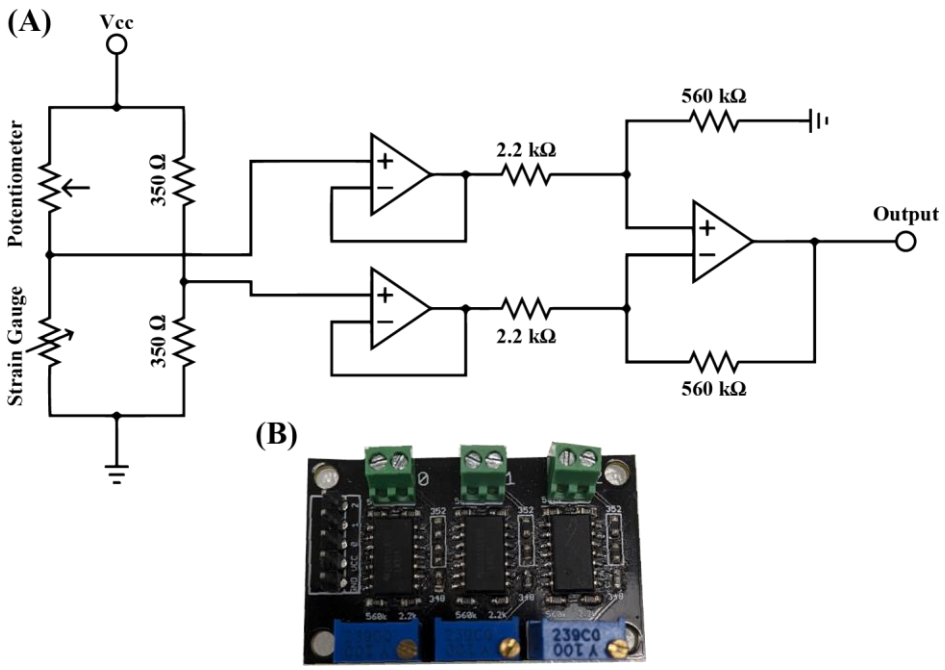

Figure 9: (A) Adjustable Wheatstone bridge and op-amp circuit, (B) PCB with three adjustable Wheatstone bridges and op-amps

3.7 Data Processing

A moving median filter with a 13-timestep window was used to filter the strain data. Without changing the strain profile over time, this filter eliminated single-step fluctuations in the data caused by electrical noise or ADC issues. This filter made it possible to reliably collect strain data that could then be used to directly simulate their sensory discharge using the CS model.

3.8 Campaniform Sensilla Sensory Discharge Model

Leg bending results in an adaptive sensory discharge from CS. Although the tonic bending moment is reflected in the discharge of the smaller CS in extracellular recordings (13), the rate of change of leg bending is encoded by a power-law function of the peak firing rate of the larger CS discharge (61). Additional dynamical characteristics of the large amplitude CS include hysteresis under cyclic bending (6,62), discharge adaptation in response to tonic bending (50), and phasic

activation in some groups when bending decreases quickly (7,63). The ability to recognize when the load on the leg suddenly increases due to gait or outside factors (61) or decreases suddenly due to foot slipping (19) is one of the dynamic responses of CS that is hypothesized to contribute to the adaptive nature of insect locomotion.

In the past, a straightforward nonlinear phenomenological model was created in which all of the dynamic responses previously mentioned could be explained by a single adaptive mechanism (8). In particular, the bending load u relative to an adaptive threshold x that follows the instantaneous bending load dominates the model output y:

$$\boldsymbol{y = \max(0, a \cdot (u - x) + c \cdot u + d)} \quad \textbf{(8)}$$

$$\boldsymbol{\tau \cdot \dot{x} = \operatorname{sign}(u - x) \cdot |u - x|^{b}} \quad \textbf{(9)}$$

where the constant parameters a, b, c, d, τ and are tuned to mimic the dynamics of animal sensory recordings. The model generalizes well, as demonstrated by earlier work. A model that has been tuned to reproduce the response to a single stimulus can also reproduce the response to different stimuli without having to change the parameter values (8). Table 3 contains the values used in this study. They are based on the large tibial CS's responses. Future research will involve gathering recordings from the trochanteral CS to use in fine-tuning the model.

Table 3: CS model parameters

Model Parameters					
Group/Parameter	a	b	c	d	τ
6B	338.9952	2.2707	7.1531	-27.9311	0.0250
6A	338.9952	2.2707	7.1531	-27.9311	0.0250
3	338.9952	2.2707	7.1531	-27.9311	0.0250
4	338.9952	2.2707	7.1531	-27.9311	0.0250

3.9 Tarsal Construction

This section provides a brief overview of tarsal construction. For more in-depth information reference Goldsmith et al 2023 (64). Three different styles of tarsi were designed each with two substyles. The substyles consist of a silicone grip at the tip, or no silicone grip attached. The silicone grips design is to improve the passive grip between the tarsus and the substrate (treadmill). Each tarsus is numbered 1-3 according to its style, as shown in Figure 10A, with an asterisk (*) to indicate the presence of the exterior silicone in the design.

Style 1, which denotes Designs 1 and 1*, is a rigid cylindrical segment that is 45 degrees offset from the tibia's long axis. Style 2 keeps the 45-degree offset and cylindrical shape, but it also features a flexible tibia-tarsus (TiTar) joint. The tarsal membranes and cuticle's elastic properties are mimicked by a ball-and-socket joint filled with silicone rubber to produce this compliance. Style 3 is a six tarsal segment design that mimics the stick insect and adds full compliance.

For the tarsal segments in the metathoracic legs of the female wild-type *D. melanogaster* (Berlin-K, RRID:BDSC 8522), nano-CT imaging from reference (29) was used to create the ball-and-socket joints. The model of *C. morosus* stepping is not anticipated to be significantly affected by modeling tarsomere joints after *D. melanogaster* because tarsal morphology is homologous among insect species (65). The joints between segments 1 and 2 and 5 and the pretarsus in the Drosophila nano-CT scans and the corresponding Style 3 designs are seen in Figure 10C-D. SEM images of the stick insect tarsus were scaled proportionally to determine each segment length (66,67). As substitutes for the pulvulli, Design 3* also includes silicone pads on the ventral side of Segments 1-4 and a pad on the pre-tarsus to represent the arolium. Due to the unguitractor mechanism's additional complexity, the claws and other active grip components are left out of this

study's designs (68). Additionally, previous research on cockroaches indicates that the removal of claws does not affect walking behavior on smooth surfaces, where the primary mechanism would be friction or adhesive pads (69).

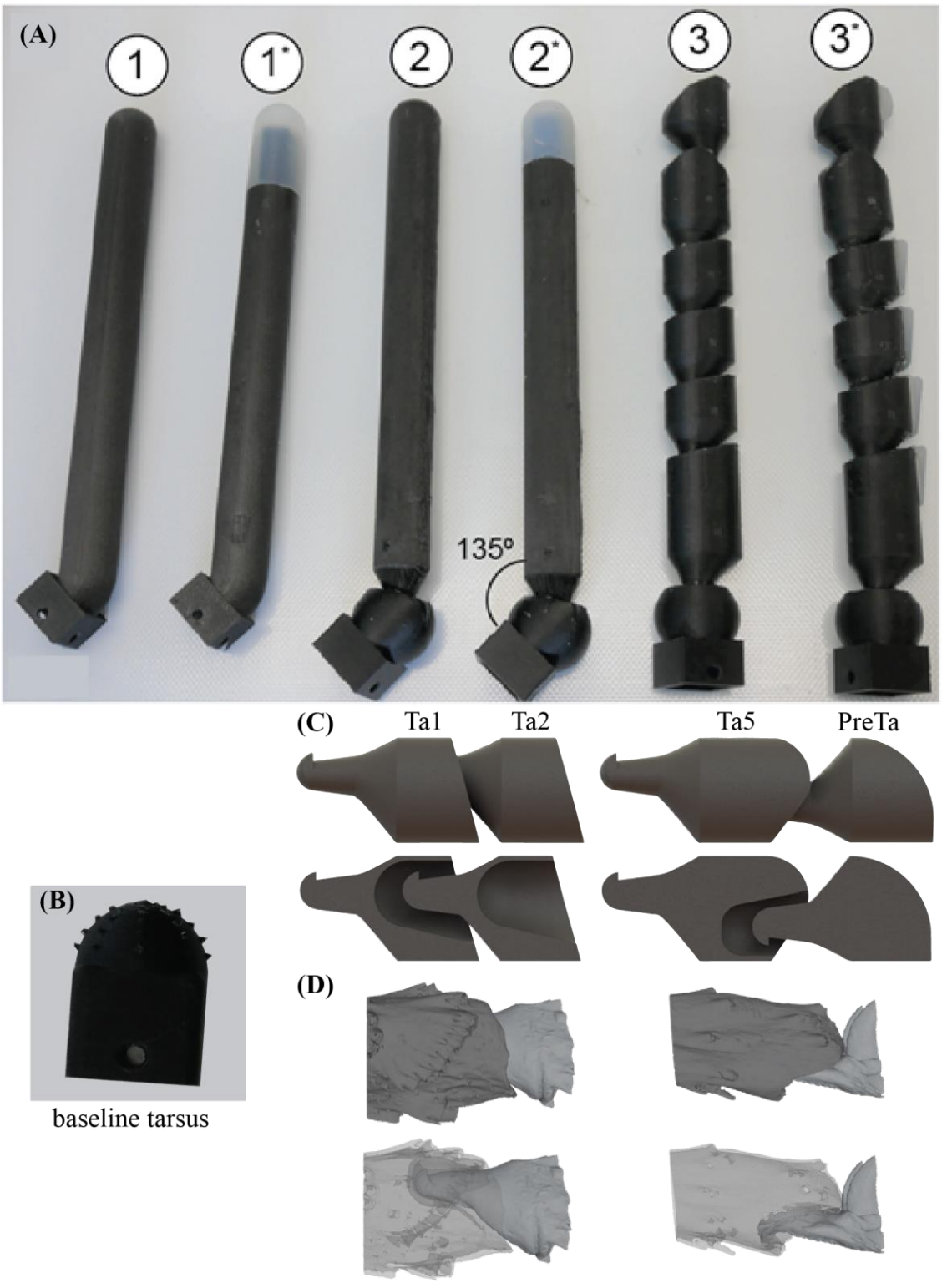

Figure 10: (A) Tarsus designs from Goldsmith et al. 2023 , (B) Baseline configuration tarsus, (C) Joint design from Goldsmith et al 2023 **(64)** (D) Nano-CT scans of *D. melanogaster* from reference **(29)**

4. Robotic Model Verification (15:1 Stick Insect)

Chapter 4 is based on my previously published paper in Frontiers in Neurorobotics (Zyhowski et al. 2023 (12)) . It was published in a special issue entitled “The Roles of Self-organization and Sensory Adaptation for Locomotion in Animals and Robots”.

4.1 Encoding of Forces

For the robotic leg model, I am interested in two characteristics of CS sensory discharge: the discharge is caused by bending loads rather than inertial forces from leg motion; and the large CS caps induce phasic sensory discharge in response to bending loads. To test these characteristics the 15:1 *C. morosus* robotic leg was used to replicate a biological experiment where an insect leg was subjected to a ramp-and-hold-and-release stimulus as shown in Figure 6 of Zill et al. 2012 (9). In the original experiment, the sensory discharge of the large CS on the leg signals the ramp portion of the stimulus and then adapts during the hold portion of the stimulus when the distal end of an insect's leg is fixed in place. The CS discharge is zero when the distal end of the leg is free. This suggests that inertial forces generated by the insect's motion are not the cause of the sensory discharge, rather the discharge is caused by bending imposed by external forces. To confirm that the lack of discharge in the unfixed case was not caused by injury to the leg, the experiment is repeated after fixing the distal end of the leg segment, and the same discharge returns. The robot's CS model discharge should have these characteristics for it to be a model of insect strain sensing.

The robot's CS model can represent the characteristics captured in the biological experiment. Figure 11 depicts the robot's CS sensors' response to a ramp-and-hold-and-release stimulus with the distal end of the leg fixed, free, and then again fixed. The strain reflects the bending moment placed on the leg segment when the distal end of the leg is fixed, and it displays a distinct trapezoidal shape over time (Figure 11B and H). The Groups 3 and 4 model CS outputs

clearly signal the beginning and end of the stimulus (Figures 11A and G). The strain output is almost zero when the leg is free to move (Figure 11E). Additionally, the zero output of the CS model (groups 3 and 4, Figure 11D) reflects this absence of strain. These findings suggest that the strain in the leg segment is not caused by inertial forces produced by the leg's motion, but rather by external forces and moments imposed by contact forces with the environment. It also indicates that the robot's motion has been dynamically scaled to correspond to that of the insect and that the robot's model discharge may correspond to the discharge that the animal experiences. Szczecinski et al. 2021's Table 3, which presents a quantitative comparison of the model discharge to the animal sensory discharge and the mean absolute error between them, provides additional support for this. The mean error for most trials is less than 10%, mean error 19.5%, and the error standard deviation is 21.9% (8).

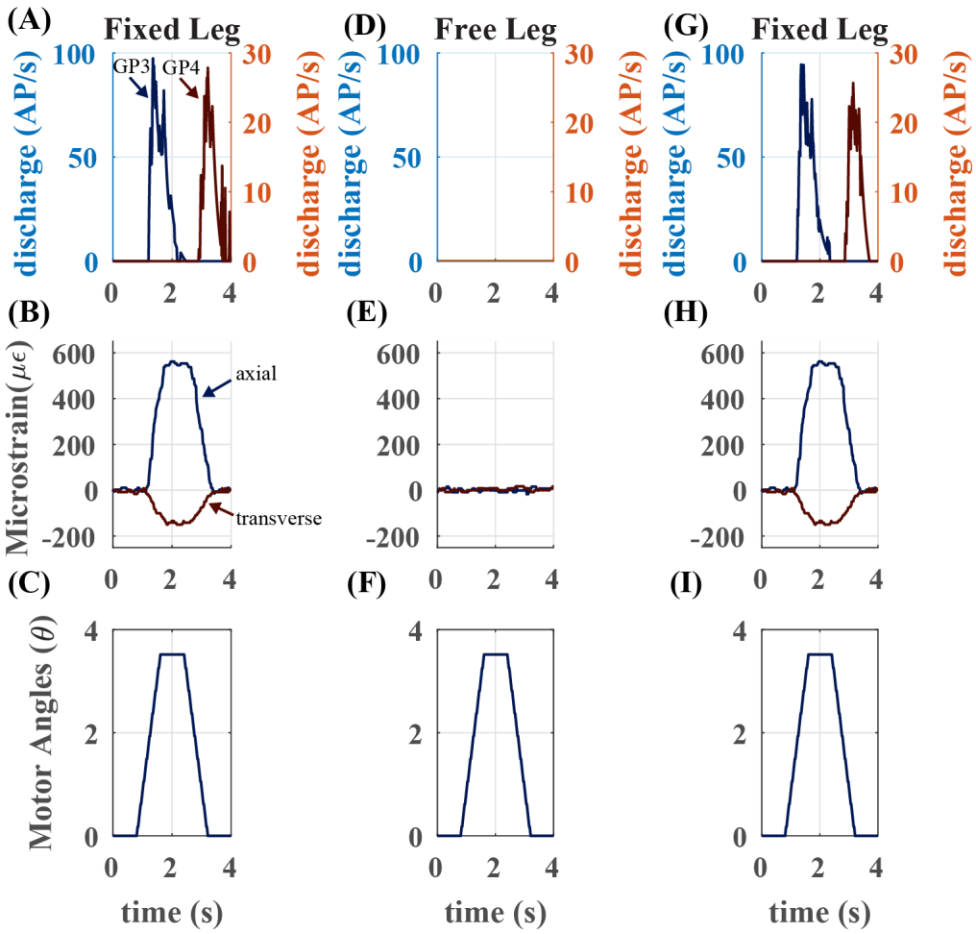

Figure 11: (A) The model CS discharge of a single ramp-and-hold-and-release stimulus with the distal end of the trochanterofemur fixed. (B) The strain of the trochanterofemur with distal end fixed. (C) Servomotor angles of the ramp-and-hold-and-release motion. (D) The model CS discharge of a single ramp-and-hold-and-release stimulus with the distal end of the trochanterofemur free to move. (E) The strain of the trochanterofemur with distal end free. (F) Servomotor angles of the ramp-and-hold-and-release motion (G) The model CS discharge of a single ramp-and-hold-and-release stimulus with the distal end of the trochanterofemur fixed. (H) The strain of the trochanterofemur with distal end fixed. (I) Servomotor angles of the ramp-and-hold-and-release motion

4.2 Baseline Operation

The trochanterofemoral and tibial CS groups' strain and model discharge are plotted in Figure 12 with four steps of output when the robot (15:1) is in the "baseline configuration," or when no weight is added. Since every step the robot took was essentially the same as every other

step, the strain and CS model discharge were almost indistinguishable step by step. The weight of the "body" creates a significant bending moment due to the orientation of this segment, which explains the largest axial trochanterofemoral axial strain. Due to the rate-sensitivity of CS discharge, the trochanterofemoral axial CS model discharge of group 3 rises quickly as stance starts. The large CS discharge model changes during the first half of the stance before becoming silenced in the middle of it. Once more, this is because CS discharge is rate sensitive. At this point, the leg's altered orientation with respect to gravity causes the strain to decrease. The trochanterofemoral transversal CS model discharge of group 4 increased at the conclusion of the stance phase which is indicative of rate-sensitive “rebound” found in insect CS sensory discharge (19). Due to the tibia's orientation, which reduces strain, a smaller version of the same condition happened with the tibial CS in groups 6B and 6A (46). The start and finish of the stance phase are clearly indicated by the model discharges which are denoted by black bars in Figure 12.

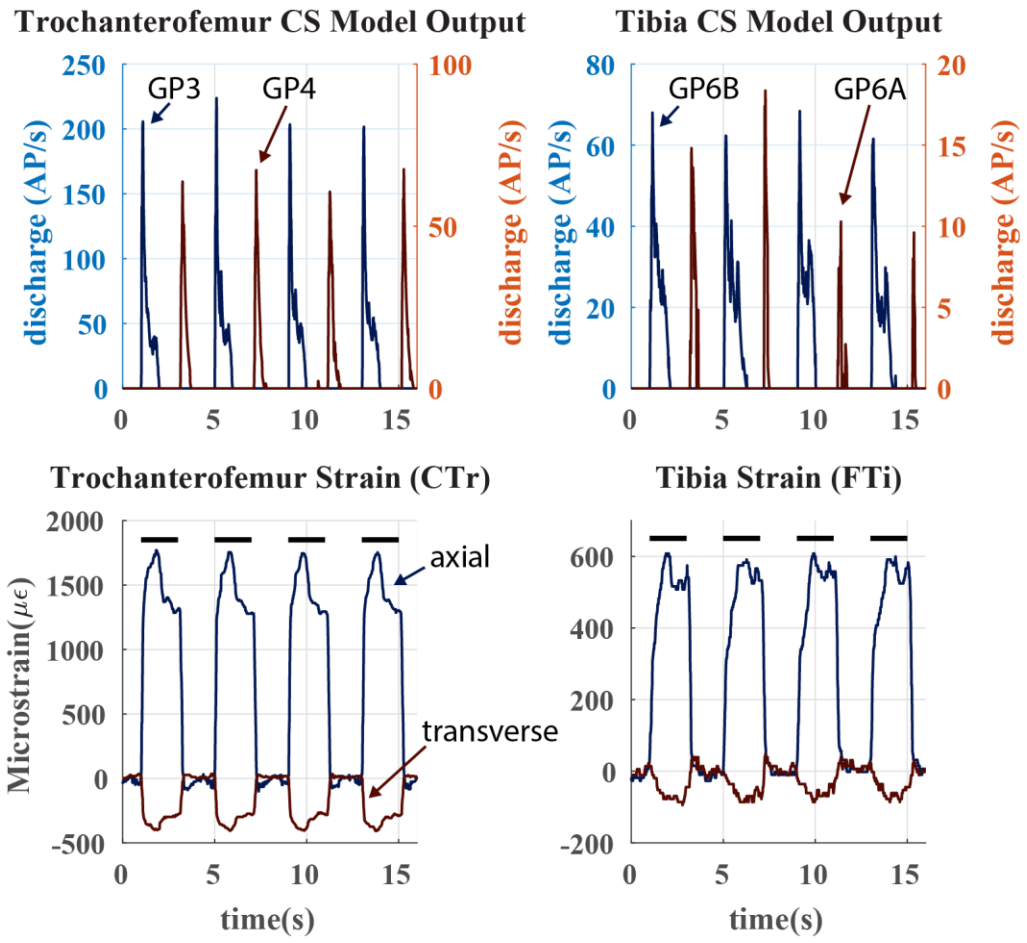

Figure 12: Recordings of middle robotic stick leg (15:1) stepping in baseline configuration. Raw strain data of 4 steps for the trochanterofemur and tibia are the bottom two graphs. Black bars denote the stance phase. Positive changes in strain denote compression; negative changes in strain denote tension. The top two graphs are CS model outputs (Groups 3, 4, 6B, and 6A). They are in line with their respective strain graphs.

4.3 Static Loading

After recording robot strain and modeling the large CS discharge as the leg (15:1) stepped on the treadmill, I added loads to the linear guide to test how changes in body weight might affect the CS discharge an insect would experience while walking. The location of the CS on the leg affected how sensitive the CS model discharge was to the amplitude of added weight. The strain and discharge from one step in each of the three configurations which are, no additional weight or

"baseline," 500 g added to the carriage on a linear slider, and 1000 g added are plotted in Figure 13 for comparison. Except for an increase in amplitude, the shape of strain for each sensor location stays mostly constant as mass is added. On the other, the tibial CS model discharge significantly alters in response to the additional body mass, whereas the trochanterofemoral CS model discharge is insensitive to it. This is probably because the CS model is rate-sensitive (8). At every location, CS groups clearly mark the start and finish of the stance phase.

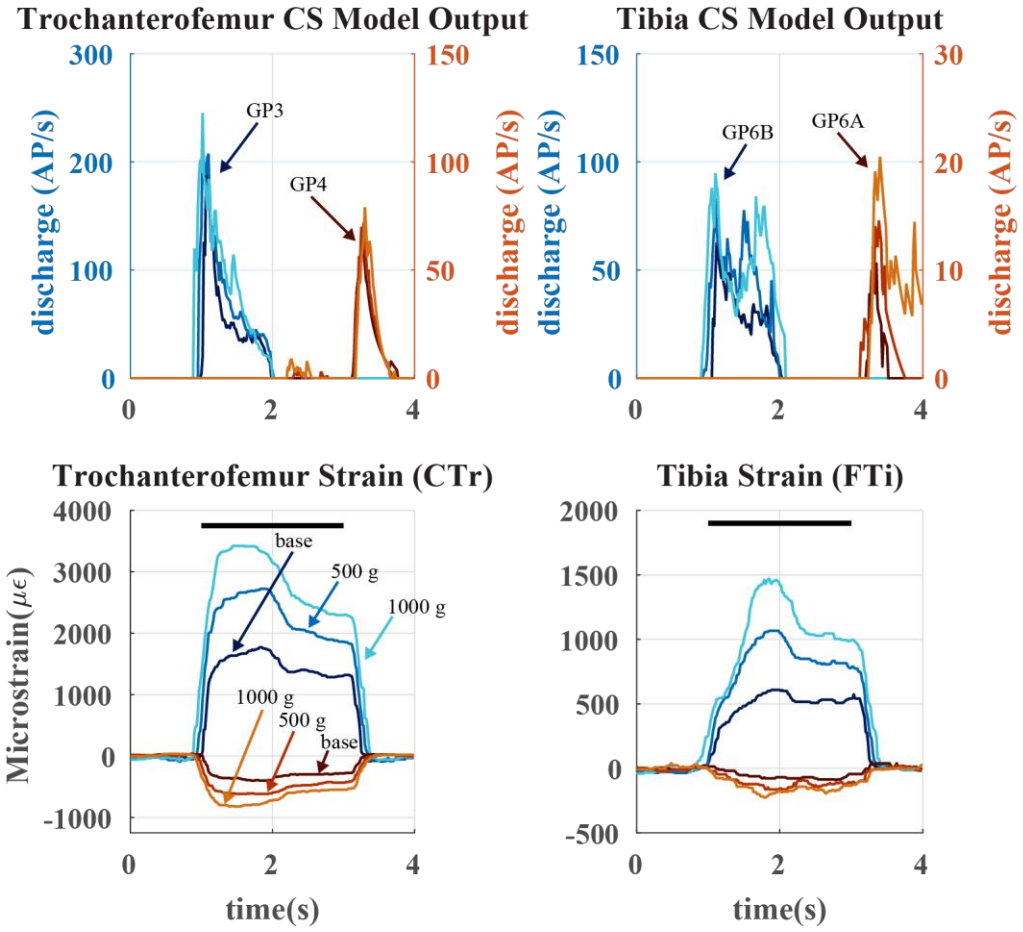

Figure 13: Recordings of the middle robotic stick leg (15:1) step in different static weight configurations (baseline, 500 g, and 1000 g). Raw strain data for the trochanterofemur and tibia are the bottom two graphs. Black bars denote the stance phase. Positive changes in strain denote compression; negative changes in strain denote tension. The top two graphs are CS model outputs (Groups 3, 4, 6B, and 6A). They are in line with their respective strain graphs.

4.4 Transient Loading

During locomotion, such as when a neighboring leg transitions into the swing phase, a leg may experience an abrupt increase in load (21,59). I imposed a transient load on the (15:1) robotic leg during its stance phase to see if CS discharge might represent these increases. The experiment involves using a second servomotor to temporarily pull the linear guide downward via a cable that is coupled to a spool. When the stance first begins, the servomotor produces a force stimulus that looks like a half sine. Figure 14 shows the effect of this stimulus on the strain. The CS model discharge is rate sensitive because it continuously tries to return to the baseline, as was already mentioned. The transient load increases the tibial strain and lengthens the period of increasing trochanterofemoral strain, resulting in an increase in the model discharge for the axial sensors of 1.5 to 2 seconds.

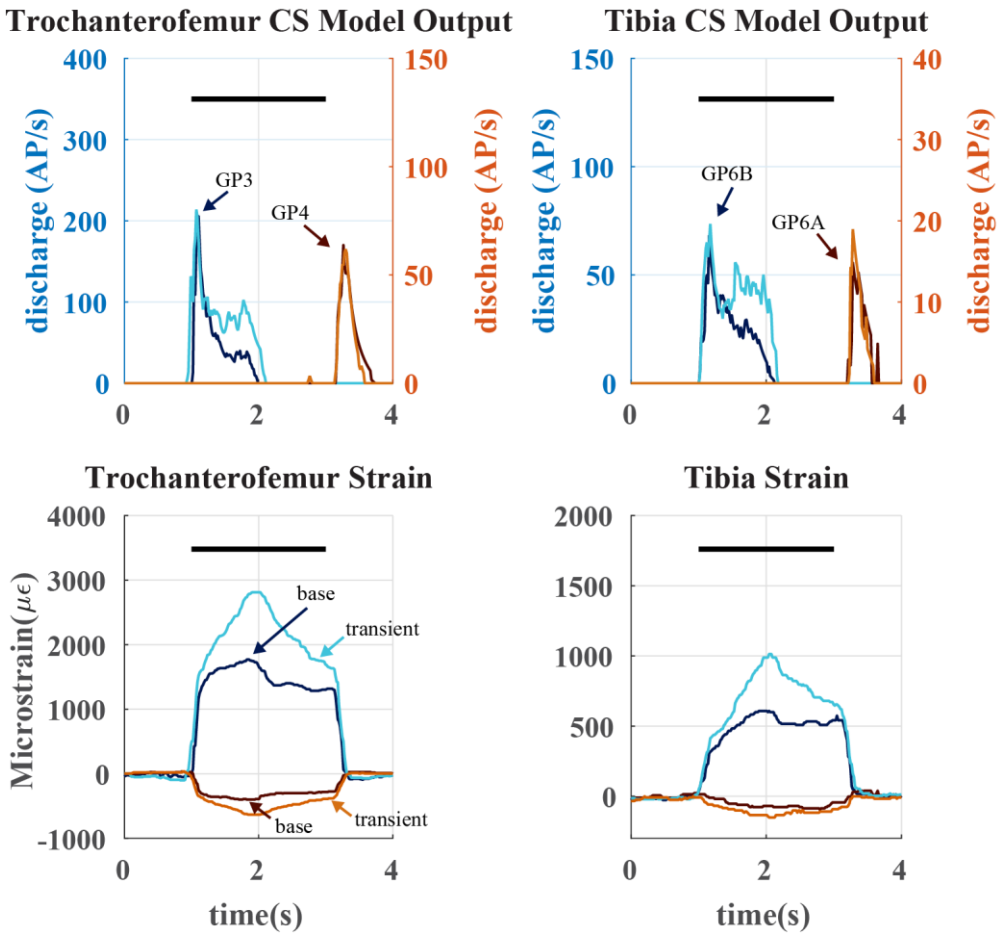

Figure 14: Recordings of middle robotic stick leg (15:1) step in two configurations (baseline, transeint weight). Raw strain data for the trochanterofemur and tibia are the bottom two graphs. Black bars denote the stance phase. Positive changes in strain denote compression; negative changes in strain denote tension. The top two graphs are CS model outputs (Groups 3, 4, 6B, and 6A) for the baseline and transient configuration. They are in line with their respective strain graphs.

4.5 Slipping Conditions

According to a recent study, a walking animal may be better able to detect tarsus slipping during the stance phase due to the adaptive nature of CS sensory discharge (19) I put this theory to the test with the robotic model leg (15:1) by causing the tarsus to slip mid-stance as the leg stepped on the treadmill. The normal walking kinematics were modified in such a way that the foot slides laterally across the treadmill surface as the tibia flexes inward and then extends outward

during the stance phase (Figure 15). The distal end of the tibia is freed when the tarsus loses contact with the treadmill, and the tibia is no longer subject to a bending moment.

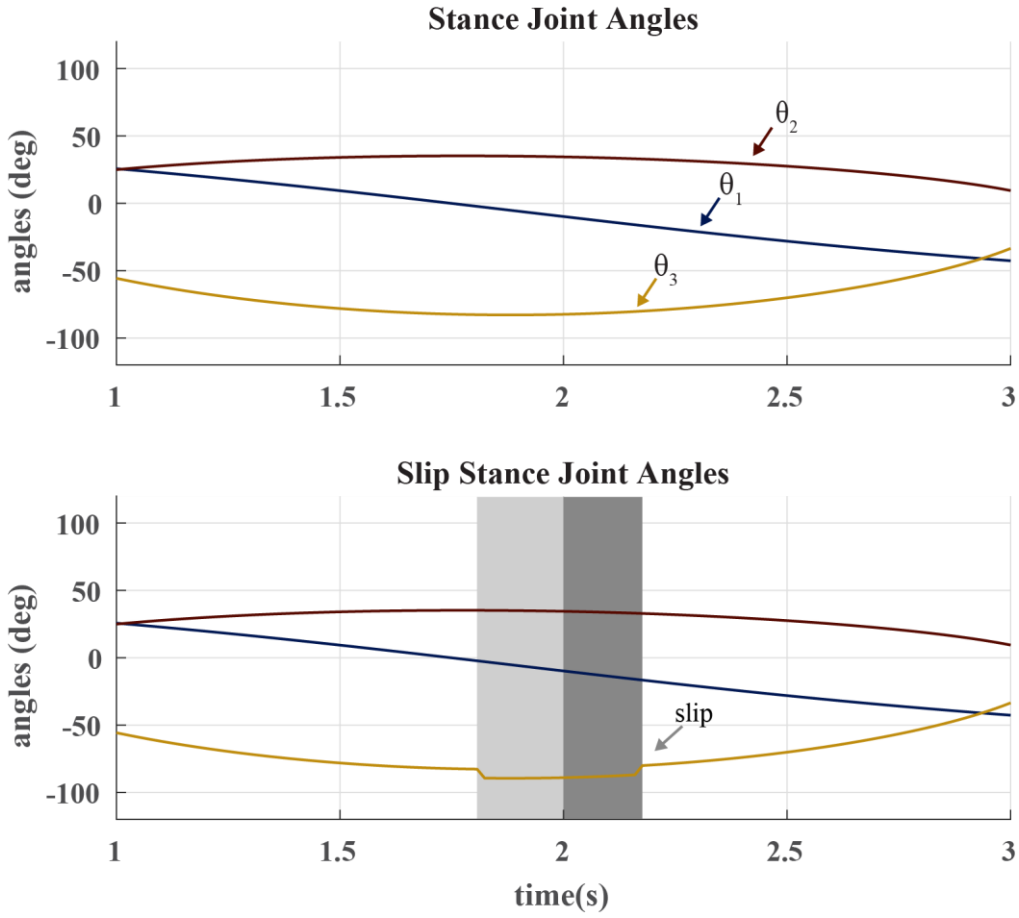

Figure 15: Standard stance joint angles and slip stance joint angles

As the bending moment on the tibia abruptly vanishes during the slip, the tibial strain drops quickly to zero silencing the axial (Group 6B) tibia CS model discharge and activating the transverse (Group 6A) tibia CS model discharge as shown in Figure 16. Normally occurring at the end of stance, this Group 6A discharge would be an unexpected signal that could trigger several motor actions, including, to name a few, a decrease in the activation of the tibia flexor muscle (70) or the initiation of the swing phase to realign the leg (71). The opposite trend is seen when the direction of the slip is changed; this results in a decrease in transverse strain and group 6B model

discharge. The trochanterofemur strain is also impacted by tarsal slip, which results in a phasic increase in the CS model discharge.

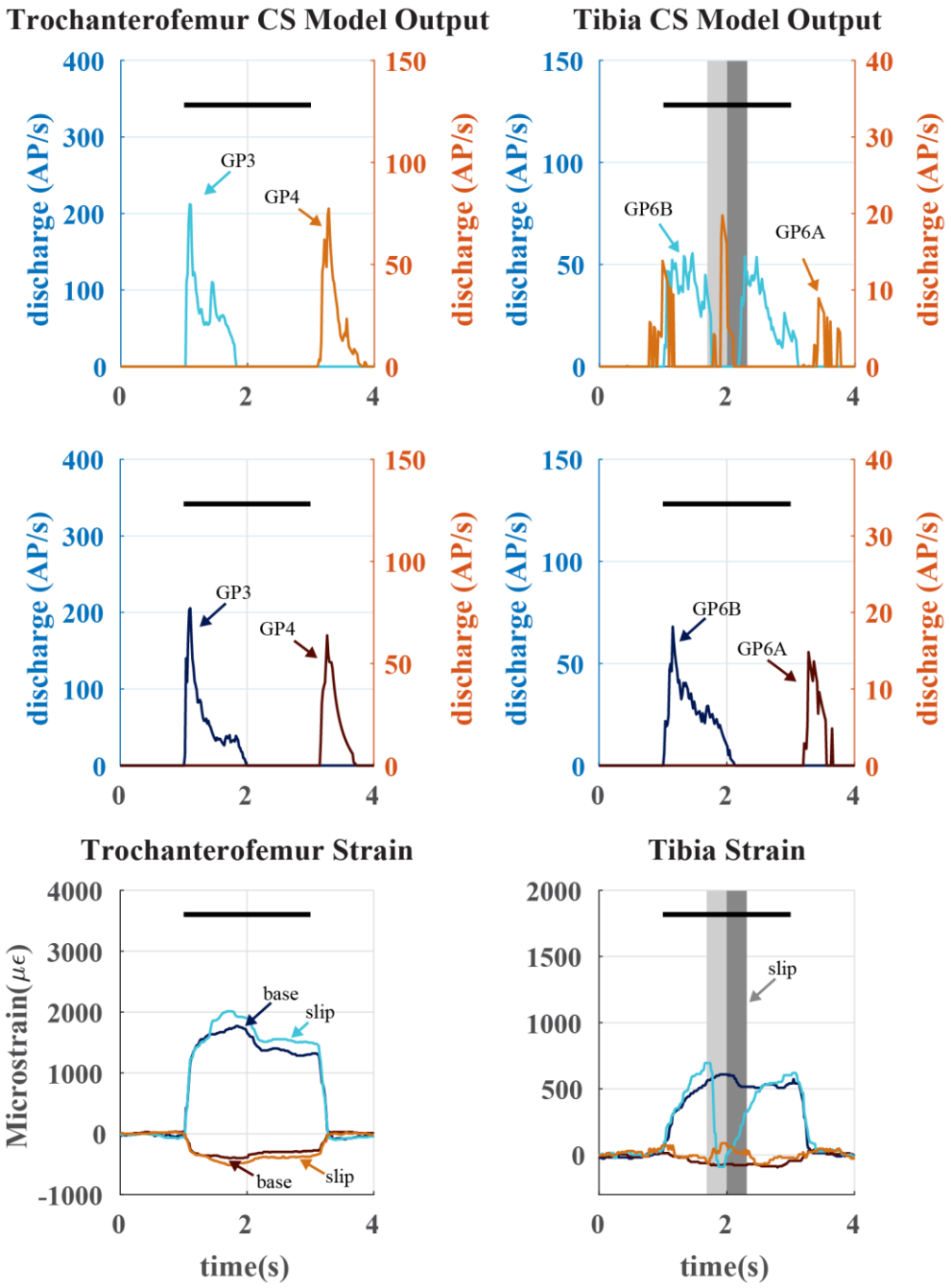

Figure 16: Recordings of the middle robotic stick leg (15:1) step in two configurations (baseline, slip). Raw strain data for the trochanterofemur and tibia are the bottom two graphs. Black bars denote the stance phase. Two tone gray box denotes the timing of forced slip. Positive changes in strain denote compression; negative changes in strain

denote tension. The middle two graphs are CS model outputs (Groups 3, 4, 6B, and 6A) for baseline configuration. The top two graphs are CS model outputs (Groups 3, 4, 6B, and 6A) for slip configuration. They are in line with their respective strain graphs.

5. Expanding the Model

Chapter 5 is based on a previously published paper in Biomimetic and Biohybrid Systems (reference Goldsmith et al. 2023 (64)). This was a collaborative effort to explore tarsal morphology on my 15:1 scale *C. morosus* robotic leg.

5.1 Robotic Tarsi

The general magnitude of the trochanterofemoral strains for Styles 1 and 3 was 25–50% greater than that observed with no tarsus in either direction as shown in Figure 17. This outcome is expected because adding an angled tarsus segment to the robotic leg (15:1) increases the moments felt by the rest of the leg by lengthening the moment arm between the ground contact point and the FTi joint. The peak strain for Style 2 was, however, about 20% lower than in both designs with no tarsus. The significant amount of deflection in the compliant TiTar joint is probably to blame for this difference. The highly flexible interior of the joint enables the joint axis to shift from the center of the "ball" to the point where the distal segment contacts the joint walls resulting in additional deflection. This kind of deflection produces elastic restoring moments, which decreases the reaction moments experienced by the limb resulting in moments that are sufficient enough to offset the negative effects of the larger moment arm angle in Style 2.

As with Style 2, Design 3* showed a decrease in the magnitude of transverse trochanterofemur strain when compared to the no-tarsus baseline. This is probably because the treadmill is the first point of contact for the Design 3* tarsus. The segments twist around their major axis to maintain anterior ground contact during stance because of the high friction between the silicone pads on the tarsus and the treadmill. As such, the blending of deflecting and rolling likely results in restorative moments that offset the increased moment arm.

For each tarsus configuration, the trochanterofemoral strains develop and weaken more gradually, producing a curve that resembles a parabola and usually peaks in the middle of stance. The tarsal moment arm is what causes this progression of strain, highlighting the effects of various leg joint angles. Design 3* stands out as the exception to this more gradual strain. The strain is highest axially right before stance, and it progressively lessens until liftoff. The strain remains mostly constant throughout the stance in the transverse direction. The high degree of grip and compliance in this design, which causes the twisting effect, is most likely what causes these strain profiles. With the tarsus fully deforming to the ground at the beginning of stance, the leg bears its entire weight, resulting in the highest strain value. The tarsus then continuously deflects and rolls in response to the ground reaction force (GRF) due to the absence of slipping, increasing restorative elastic axial moments. The initial position of the tarsus during stance creates a constant transverse moment arm, resulting in a largely constant transverse strain.

The tibia strain data showed some effects from applying a tarsus that wasn't seen elsewhere. The strain readings became much more sensitive to the pronation/supination of the leg, especially in the transverse direction. This meant that for Styles 1 and 2, the tarsus tip began the stance positive and turned negative as it approached the posterior aspect of the FTi joint. The Design 1* strain is where this is most visible. Contrary to the no-tarsus design, where axial and transverse strains are scaled opposites and consistent with simple tension or compression of the leg surface, this strain propagation is unbalanced. Every tarsus style, however, disrupted this inverse scale relationship, causing axial torsion to occur along the tibia. The only tarsi design that produced purely positive tibia transverse strain throughout the stepping cycle were those in Style 3. These tarsi's twisting behavior may be the cause of this occurrence.

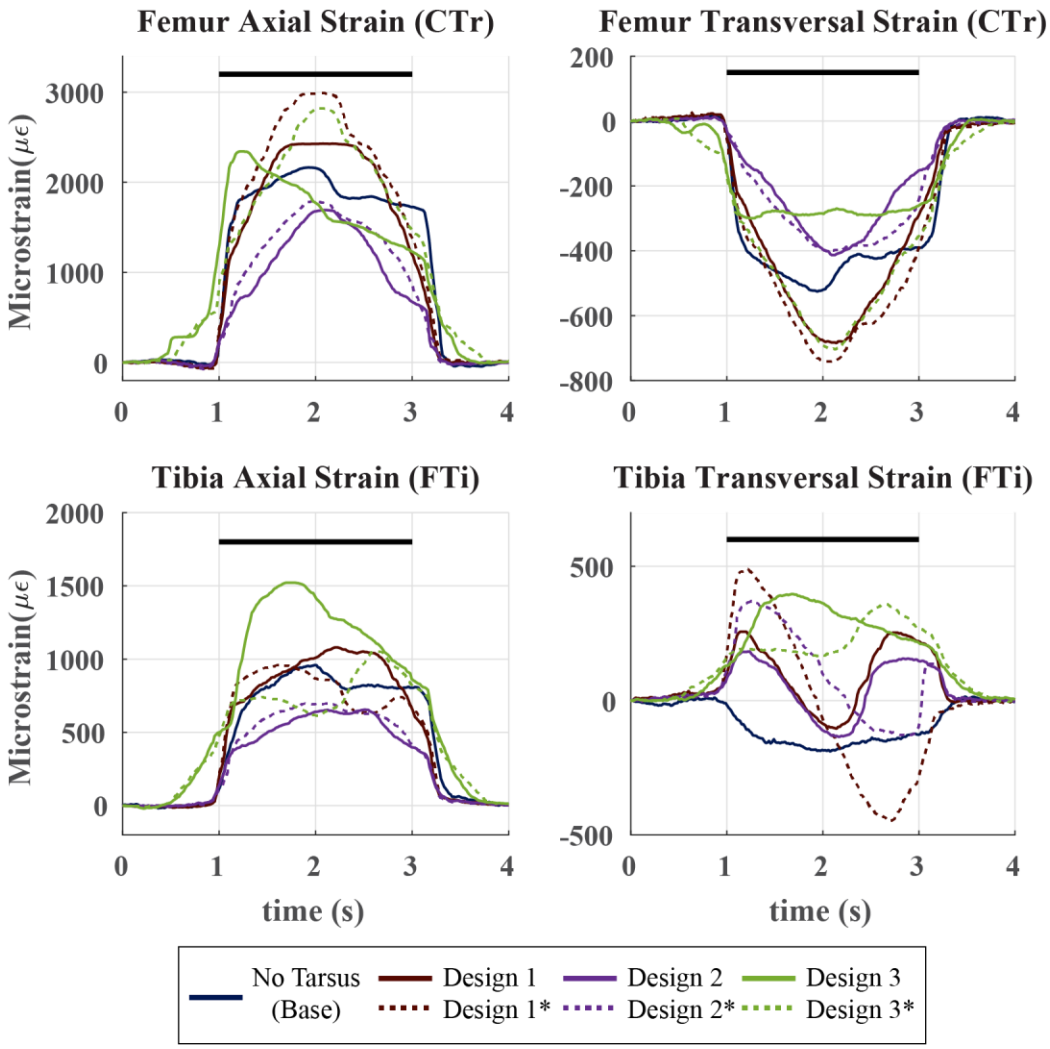

Figure 17: Recordings of strain for middle robotic stick leg (15:1) for an average step for each tarsal design. Each design is denoted with a specific color. Designs without silicone grip are solid, while those with silicone grip are dashed. Black bars denote the stance phase. Positive changes in strain denote compression; negative changes in strain denote tension.

6. Expanding to Other Model Insects

Chapter 6 is based on a previously published paper in Biomimetic and Biohybrid Systems (reference Dinges et al. 2023 (47)). This was a collaborative effort to expand the model to a *D. melanogaster* leg and compare similar CS morphology to that of the *C. morosus*.

6.1 Comparison of Stick (*C. morosus*) and Fly (*D. melanogaster*) Strain

The strain was measured on two robotic legs (*25:1 C. morosus,* and 400:1 *D. melanogaster)* while stepping at three different speeds in order to examine how variations in stepping speed impact leg strain (Figure 18). The stance phase's duration (2 s, 4 s, 6 s) was changed to modulate the speeds, which is in line with how insects adapt their walking speed. The walking speed is indicated by a black line for 2 s swing, 2 s stance, a gray line for 2 s swing, 4 s stance, and a light gray line for 2 s swing, 6 s stance.

During the stance period, distinct strains were detected at the G2 transverse and G2 axial strain locations on the anterior face of the leg. G2 transverse detected strain decreases in the robotic leg, peaking at the start of the stance phase. With a brief peak at the end of the stance, the strains gradually decreased over time. The inverse is detected in the G2 axial gauge in contrast to the G2 transverse. At the beginning of the stance, the strain gradually increased and peaked at the end.

Tensile strain was detected on the dorsal leg face with peaks in intensity at different times during the stance phase on the more transverse G3 and the more axial G4. Comparable to G2 axial, G3 in the model started encoding strain at the start of stance and peaked at the conclusion of stance. During the stance phase, compressive force was applied to this location; the compression was highest at the step's conclusion. Compressive strains were also felt by G4 during the stance phase. In contrast to G3 the beginning of stance as opposed to the end was when it was most stressed. There was a gradual decrease in strain after this stance peak, with an additional, smaller increase

at the end. G1 is mostly oriented transversely and is found on the posterior leg face of *C. morosus*. Here, G1 and G4 detected strain during stepping in a similar manner, with a primary peak at the beginning of stance, a gradual decline, and a smaller peak at the conclusion of the step.

The anterior leg face of the fly model has no CS, while the CS nearest to the anterior face was the TrF transverse, which peaked at the beginning of stance. Throughout the remainder of the stance phase, the strain progressively decreased without increasing again at the end of the step. TrF axial refers to the more posterior subfield of the TrF. In the model, this location also detected the highest strain at the start of the stance phase, similar to TrF transverse; however, it detected tensile forces rather than compressive forces. Moreover, there were no more peaks in the strain throughout the remainder of the stance, only a steady decline.

Compressive strain was detected at the TrG joint, the only CS location found on the fly's trochanter. Comparable to the TrF transverse, that location underwent compressive forces and experienced increases in strain, which peaked at the beginning of the step. Throughout the remaining stance phase, the strain measurement did not reach another peak.

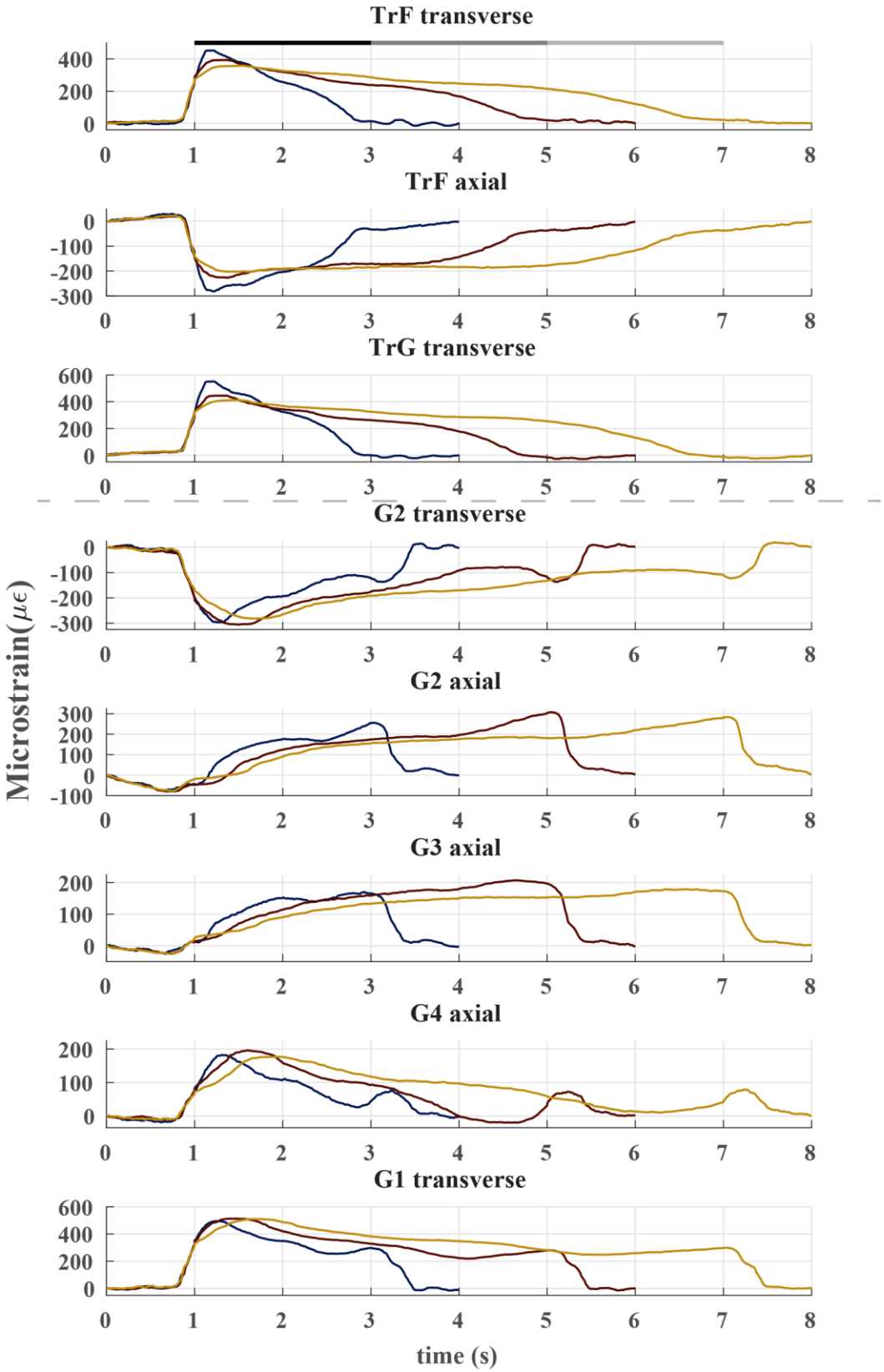
TrF transverse
TrF axial
TrG transverse
G2 transverse
G2 axial
G3 axial
G4 axial
G1 transverse
Microstrain($\mu\epsilon$)
time (s)

Figure 18: Strain recordings of robotic fly (400:1) and stick (25:1) middle leg at different stepping speeds. Black line denotes 2 s swing, 2 s stance, gray line denotes 2 s swing, 4 s stance, and light gray line denotes 2 s swing, 6 s stance. Postitive changes in strain denote compression; negative changes in strain denote tension. Fly strain (top graphs) and Stick strain (bottom graphs) are seperated by light gray dashed line.

6.2 Comparison of Undetected Strain

Strain was measured on both robotic legs (*25:1 C. morosus*, and 400:1 *D. melanogaster)* in artificial sensor locations and both axes of existing CS groups to examine what would be measured by CS locations that are present in some species but absent in others (Figure 19). This included the posterior transverse sensors' perpendicular posterior axial subfield in the stick insect. The fly's additional CS groups were on the anterior face and were mirrored in relation to those on the posterior face. These are referred to as anterior transverse and anterior axial. A sensor designated as the posterior axial sensor, which is perpendicular to the posterior transverse location was added as well. A two-second swing and two-second stance phase was used as the step period for this experiment.

The only sensor location lacking two subgroups in the stick insect is the posterior face, where axial CS does not occur. Throughout the stance, the strain gauge registered a comparatively constant amount of strain, which peaked at the conclusion of the stance phase. The strain data was in line with the G3 group.

Three fabricated locations in the fly model leg are utilized. Mirroring the orientation of the posterior face strain gauge, an anterior face strain gauge was affixed to the limb. The posterior transverse strain gauge's perpendicular axis served as its artificial subgroup as well. The measured strains peaked at the start of stance at all locations, comparable to the fly model. The anterior transverse and posterior axial groups mirrored the strains seen at TrF axial. A similar output was also seen in the anterior axial sensor.

In contrast to the fly, the stick insect has anterior CS locations. However, the strain that the stick insect's anterior transverse field perceived was also detected by the artificial anterior transverse location G2. However, the fly's artificial anterior axial sensor did not track the same strain as the stick insect's G2 anterior axial sensor did. Whereas the stick insect had tensile force, the fly had compressive. Moreover, the stick insect's anterior axial sensor was strained more at the end of stance than the fly's anterior axial which is strained at the beginning.

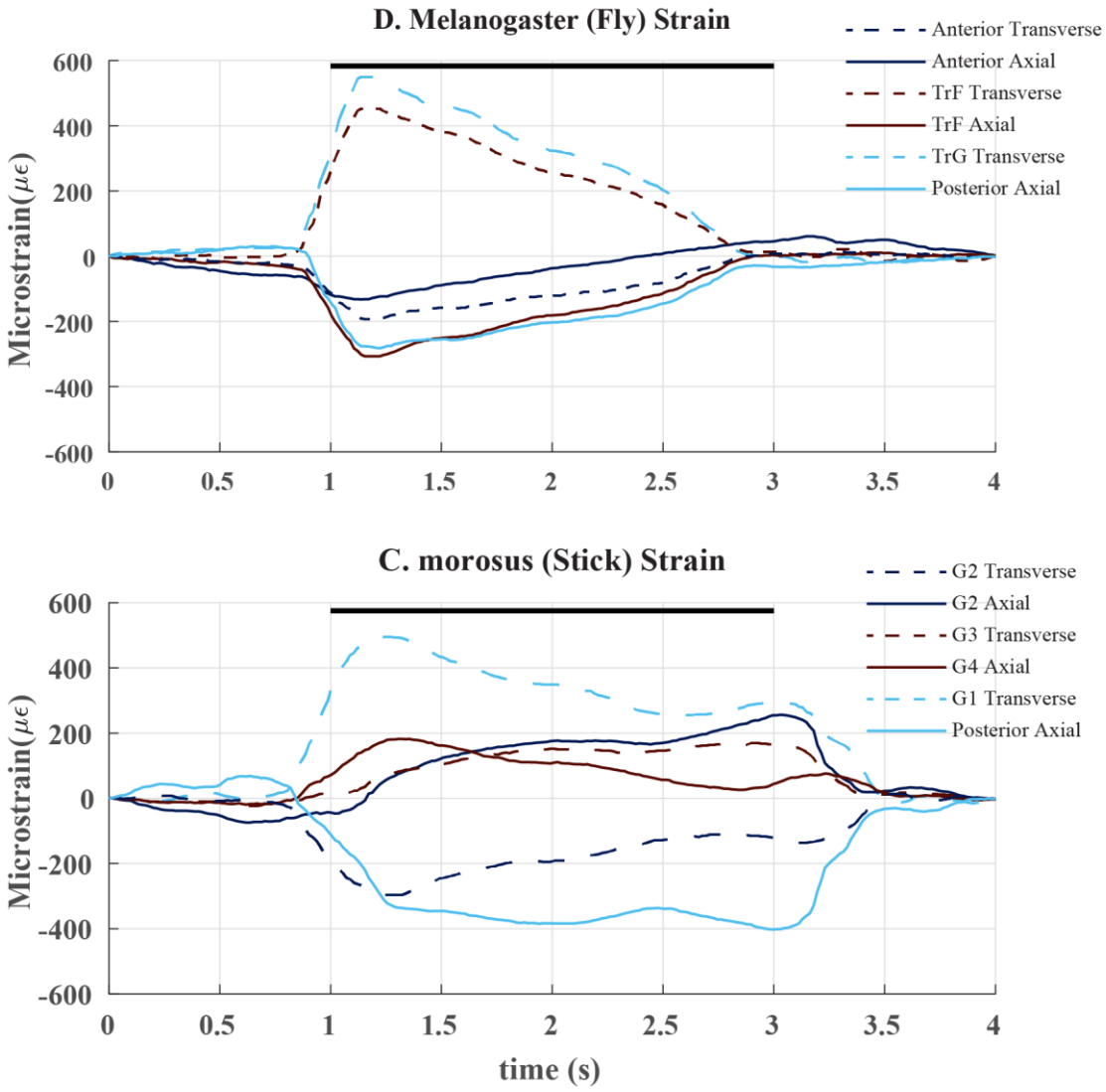

Figure 19: Strain recordings of robotic fly (400:1) and stick (25:1) middle leg with added artificial CS locations. Artifical locations are anterior axial, anterior transverse, and posterior axial on the fly leg. Artificial locations are posterior axial on the stick leg. Black line denotes stance. Postitive changes in strain denote compression; negative changes in strain denote tension.

7. Discussion

7.1 Discussion Summary

This work is based on multiple previously published papers (for reference (12,47,64)) through work of my own and collaboration with my lab colleagues. In Section 7.2, I discuss my 15:1 scale *C. morosus* robotic leg and explain how I verified its usefulness as a model through various forms of testing. The model is further expanded upon by adding different tarsus designs in section 7.3. Section 7.4 involves the loading comparisons of the 25:1 scale *C. morosus* and 400:1 *D. melanogaster* robotic legs. Section 7.5 discusses the applications these types of robotic models have and how incorporating load sensing could improve the implementation of future robots. I address the robustness of the model in section 7.6. Section 7.7 discusses how these model types compare to the real biomechanics and neurophysiology of the actual insects. The limitations of this study are described in detail in Section 7.8, along with potential future solutions.

7.2 Robotic Stick Insect Leg

In Chapter 4 I compared the robotic 15:1 scale leg to that of a stick insect which verified this robotic modeling approach with biological experiments and investigated what force signals the insect's nervous system might be encoding in more complex scenarios. Strain gauges were positioned on the robotic leg in four orientations that paralleled the main CS groups (Groups 3, 4, 6A, and 6B) found on stick insect's middle leg. Tests that mimicked the responses of biological CS receptors were carried out on the mechanical leg. Once it was determined that the force encoding of the robotic model matched that of the animal, I used it to simulate a sensory discharge that would occur *in vivo* during an animal's gait. By perturbing the leg with constant and transient loads and causing its tarsus to slip, it was possible to gain insight into how CS in the animal may

signal such conditions. As a result, this study can offer special insights into the different kinds of force signals that the stick insects experience and how this information might be applied to the control of a walking robot.

The CS model discharge highlights the dynamic changes in force that take place at the start and end of the stance phase, similar to the CS discharge of insects (19,71). This is due to the model discharge's high sensitivity to the rate of force change, similar to the sensilla discharge (15). The coordination of walking in insects depends on detecting the beginning and end of the stance phase (13,59,72,73), emphasizing the significance of CS and their sensory discharge dynamics. I speculate that compared to a walking robot without such filtering, one with it might have better interleg coordination. Future research using six-legged robots and closed loop control will investigate this.

There are several ways that insects appear to make use of CS sensory feedback. All leg CS are responsive to force dynamics, and experiments with joint torques obtained from animals that are free to walk (16) show that rather than just encoding the force level, the receptor discharges reflect the rate of change of forces (15). To ensure efficient walking motions, these signals could be used to modify muscle activity and account for force variations. For instance, tibial CS (Groups 6B and 6A) feedback may be used to modify the output of the leg muscles in order to prevent tarsus slipping while walking (70). On the other hand, at the start of the stance phase, feedback from the trochanteral CS (Groups 3 and 4) may increase muscle activity and quickly produce support and forward motion (9). These results suggest that the CS receptor signals are used adaptively depending on the receptor location and the behavior being carried out. Due to the challenge of simultaneously recording from so many CS in a moving animal, it might be challenging to directly confirm the function of such feedback. While it might not be feasible to carry out these tests on

the insect, the robotic leg is not constrained by these issues, so I can conduct further research on the leg to investigate load feedback in insects.

7.3 Tarsus Implementation

In order to investigate the impact of tarsi on strain readings, tarsi were designed and implemented on the 15:1 scale robotic *C. morosus* leg in Chapter 5. To isolate morphological effects, these tarsi were developed with differing degrees of compliance, passive grip, and biomimetic structure. Silicone-based compliant tarsal joints were created to mimic the elasticity of the animal's tarsal cuticle and joint membranes. While the leg stepped on a treadmill, I measured the trochanterofemoral and tibial strains in both axial and transverse directions. Next, I calculated the average profiles of strain over several steps and found that the strain profiles throughout the leg showed several discernible effects from the addition of a tarsus (Figure 17). Because a tarsus adds a moment arm between the ground contact point and the leg joints, the overall magnitude of the strains is generally increased. Compliant components with sufficiently large deflections may counteract this effect and result in strains that are smaller than the baseline. In many cases, the tarsus-induced moment arm also increased the sensitivity of the femur strains, resulting in more gradual growth and decay of the strain over the stance phase. As the tarsus tip moved along the body plane, the angling in two of the designs in the tibia caused the tibia transverse to change signs midway through stance. Passive grip seemed to increase tibia transverse strain and inhibit slipping in these experiments, but it had little effect on femur strains.

In Style 3, the strain deviated from several of the general strain trends with the most biomimetic tarsus designs, especially when it came to adding grip. Unlike Styles 1 and 2, where the tibial transverse strain changed from tension to compression during stance, Style 3's designs maintained compressive tibial transverse strain throughout. In Design 3*, femur strain peaked at a

different time than in the other designs, and it was less in the transverse direction than in the case without a tarsus. This behavior could be a result of increased ground contact and grip in this style, as well as a far higher degree of compliance. The grip in Styles 1 and 2 was enhanced by the addition of a silicone tip, but the ground contact area stayed small. Style 3 did not have this problem because of its compliance, which greatly increased the contact area and allowed more segments to touch the ground. This design was then able to twist and bend to great degrees throughout stance to maintain its initial point of contact with the treadmill, especially with pulvulli included. This resulted in the creation of unique moment arms and elastic restorative moments. The tarsus of stick insects has been observed to undergo a comparable degree of deformation when they walk, suggesting that the behavior of this design may further support its biomimicry rather than be a drawback (74). The divergences between the most biomimetic designs and the patterns found in more abstract segments point to a complicated interaction between ground force mechanisms in the tarsus that will take more investigation to fully understand.

7.4 Comparisons of Stick and Fly Robotic Legs

In Chapter 6 strain changes that occurred during stepping in two dynamically scaled robotic legs that were adapted after the morphologies of two model organisms for motor control: *D. melanogaster* and *C. morosus*. The legs of *D. melanogaster* and *C. morosus* were scaled to the insect at a ratio of 400:1 and 15:1, respectively. Comparative studies, in my opinion, help us better understand how homologous organs may be impacted by species-specific morphology as well as proprioceptive function. The strains that the strain gauges picked up indicated that both robotic legs had entered stance. Only the *C. morosus* robotic leg model had sensors in places that were sensitive to strains that arise at the end of stance which is consistent with recordings of stick insect CS groups (9).

While G2 axial and G3 peaked at the end of stance, the stick insect's G2 transverse, G4 transverse, and G1 transverse registered strain peaks at the beginning (Figure 18). TrF transverse, TrF axial, and TrG all peaked at the start of stance in the *D. melanogaster* model; no additional peaks occurred at the end of stance. This indicates that while the fly's trochanteral CS primarily monitors the onset of stance, trochanteral CS locations in the stick insect monitor different phases of the stance phase. Furthermore, the stick insect leg model demonstrated similarity between nearby locations during sensor activity, which indicated the strain detected between the beginning and end of stance. The peak tensile force was detected at the most anterior location (G2 transverse). At the end of stance, compression was detected by both its dorsal neighboring field, G3 transverse, and its subfield, G2 axial. At the onset of stance, compressive strain was detected by G4 axial, the subfield of G3 transverse, and by G1 transverse, its posterior neighboring field, at the same time. The artificially positioned G1 axial felt tensile force, much like the G2 transverse, but it displayed distinct dynamics, with an extreme at the end of stance (Figure 19). With two nearby fields monitoring the same strains in a posterior-to-anterior tracking of the start to finish of stance, this pattern of strain monitoring points to a phase shift-like progression in field activity.

In contrast to the stick insect model, all sensor locations in the robotic fly leg, including the artificial locations, registered the highest strain at the beginning of stance (Figure 19). Changes in body size could impact these underlying differences. Wing CS of larger insects with lower wingbeat frequencies, for instance, served as magnitude detectors in CS investigations, whereas the CS of smaller insects with higher wingbeat frequencies fired only once during the wing stroke (75). In this sense, the primary sense that larger insect sensors picked up on was force magnitude, while smaller insect sensors picked up on timing. Along with shorter wingbeat durations, *D. melanogaster's* faster average stepping in comparison to *C. morosus* may also lower their capacity

for temporal integration, which would require less monitoring of the start of the stance phase (45,75–77).

The distinct leg posture, specifically the way each leg is extended and supinated during stance, may also account for the observed variations in load variation between species. Longer legs generally result in higher moment arms of ground reaction forces at the foot, which should put more strain and stress on the proximal portions of the legs. The strain gauges will also become misaligned from the axes of the predominant stresses if the leg is pronated or supinated because CS and strain gauges are directionally sensitive. These effects mix differently in every animal because their stepping motion is different. Additionally, the *D. melanogaster* robotic trochanter's accessibility limited the study. The placement of the trochanteral CS on each leg's femur caused the legs to further alter CS orientation as they walked. Subsequent studies will expand the Drosophila robotic trochanter to suit the required CS and investigate the effects of the moving trochanter-femur joint on load sensing in more detail.

The leg of the stick insect extends to the beginning of stance, flexes during the first half of stance, and then extends again during the second half of stance to reach the end of stance (53). Because of this, the ground reaction force's lever arm on the body initially increases, then decreases, and finally increases. Concurrently, the leg plane pronates and supinates during stance, resulting in stresses that are not aligned with G4 axial at first, aligned with G4 axial mid-stance, and misaligned at the end of stance. A relatively constant but ultimately "dual-peaked" profile can be seen in the stick insect G4 axial recording as a result of these mechanisms.

The leg of the fruit fly, on the other hand, stays flexed as it approaches the beginning of the stance and then extends to the finish. Moreover, the leg begins and ends in a supinated position rather than being pronated or supinated. The "dual-peaked" strain profiles observed in stick insects

are not produced from flexion to extension and from neutral to supination. Rather, every fruit fly recording is "single-peaked." These posture variations would undoubtedly alter how stress is applied to and resisted throughout the leg, even though the legs of both species serve the same functions of supporting and propelling the body. As was previously mentioned, variations in locomotion speed may be the cause of such postures. There may be more extensive relationships between these morphological and behavioral characteristics if an evolutionary and developmental survey of insect species, their leg posture, their locomotion rates, and the location of their CS is conducted.

The reason Drosophila has fewer CS locations on its trochanter and the stick insect lacks a G1 subfield could potentially be attributed to the variations in the two legs' sensor location leg functionality, as previously mentioned. The missing locations would also monitor tensile force at the start of stance, which is what the axial trochanter field of the *D. melanogaster* model would have detected. Similar strain developments were detected by the stick insect model's G3 transverse, which was compressed during the stance phase and had a posterior axial subfield missing. Furthermore, the stance phase exposed all "missing" locations to tensile strain, which might not have resulted in CS activity (51). It should be noted that the use of strain gauges to simplify the sensor field placed limitations on the current endeavor. Certain sensors may activate at different times due to variations in the precise orientations of the caps within each field.

This experimental method could be used in future research to infer, from the leg orientation and walking kinematics of the species, which CS fields and groups other insect species have. The main hypothesis is that CS fields and groups that redundantly signal loads might have disappeared over evolution. Further investigation into the behavior of individual species may point to additional causes for the evolutionary changes in CS fields and groups.

7.5 Applications in Robotics

The dynamic CS discharge model in Chapter 4 could make it easier to build and run robots with numerous redundant sensors, much like insects do. Robots frequently employ a minimal number of sensors to determine the complete state of the robot. This approach is used for practical reasons because it is difficult to configure and calibrate sensors on a robot to function reliably. The control hardware may use more power as a result of this method's increased computational load, which could reduce the amount of time the robot can operate before the batteries are depleted. Additionally, it raises the question of how small animals with limited resources, like insects, can carry out the intricate calculations thought to be required to operate legged machinery. By incorporating sensors that directly measure quantities of interest acting on the leg, insects and consequently robots may reduce the complexity of calculations required for control. In contrast to sensors that measure the forces of individual muscles, like Golgi Tendon Organs or individual motors, like current sensors, insect CS may make controlling the leg easier by signaling forces produced by groups of synergistic muscles, as stated in the early study of Pringle (1). Although adding sensors to the robot may make it more complex, the dynamic CS model's robust signaling of load increases and decreases may make calibrating these sensors easier. It will be interesting to see if this method makes it easier to process data from redundant robot sensors. The intent is to use this strategy in subsequent research on hexapod robots, each of whose legs are instrumented similarly to the robotic leg used in this study.

To be more precise, dynamic load feedback processing may improve the interleg coordination of walking robots. It is well known that the load carried by each leg affects the coordination between the legs in insects and other arthropods (13,37,59,72). Animal locomotion is supported by neuromechanical simulations (37,44,78) as well as robotic models (42,43). But as

far as the authors are aware, no earlier study has integrated the dynamics of how CS measures load into their robot controller. It can be challenging to adjust strain sensors so that they don't produce erroneous leg load readings, both positive and negative. I believe that the adaptive nature of the CS discharge model I have used will make it easier to accurately determine when the leg is in swing or stance, which should improve interleg coordination in robotic applications.

Dynamic CS discharge modeling may also help with interleg coordination of robot leg control. It is known that the patterning of the motor output that controls other leg segments is influenced by the feedback from CS on one leg segment (79). Dynamic neural models (44) or abstracted finite state machine controllers (80), in which the motion of each joint is dependent on load feedback from across the leg, have been used as robot controllers to mimic this mechanism. By providing precisely timed, high-amplitude signals when the tarsus contacts the substrate, dynamic CS discharge may aid in such intraleg, intersegmental coordination. This could be investigated by integrating the CS model into the closed-loop control of a walking robot,

7.6 Model Robustness

The nature of the CS model in Chapter 4 ensures that the feedback remains robust to variations in loading. Robots experience a wide variety of unpredictably sensory stimuli, much like insects do. My experiments show, for instance, that the trochanterofemoral CS discharge in Figure 13 is not affected by variations in loading. The models' output consistently identified the start and end of the stance phase in each of the cases that I tested. This indicates that the adaptive strain processing carried out by the CS model would increase the robustness of a control network that sets the timing of each joint's motion.

In certain cases, extra leg load information was encoded, despite the fact that the model discharge was robust to changing load conditions. In Figure 16, Group 6A, for example, discharged

when the foot slipped and the tibial strain rapidly decreased to zero, indicating that the tibia was no longer being strained. The trochanterofemoral strain increased at the same time. The CS model's adaptive properties cause it to emphasize load variations over time, signaling when the motor control needs to be modified.

7.7 Comparison to Biomechanics and Neurophysiology

The signals from the strain gauges closely matched those found in CS after filtering and processing. The mathematical CS model could process the measured strain to produce animal-like signals in response to both increases and decreases in force such as in Figure 12. Similar to biological receptors, strain gauges enable directional force reception. Moreover, processing strain measurements using the CS model might mimic the diverse degrees of adaptation present in biological sensors, especially the remarkable adaptation of large receptors to tonic forces. As a result, the robotic leg successfully imitated some aspects of CS discharge in insects.

The model's ability to accurately distinguish between the beginning and end of the stance phase is one distinguishing feature. The model outputs demonstrate this, with groups 3 and 6B increasing amplitude at the beginning of stance and going silent as the force decreases. After a brief period of silence and increasing at the end of stance, Groups 4 and 6A exhibit the opposite trend. These outcomes closely resemble CS as it has been observed in insects (7,13). In contrast to the smaller CS, whose discharge adapts less than that of the larger CS, it is significant to note that the model mimics the characteristics of the larger CS (11). When animal legs are subjected to ramp-and-hold-and-release stimuli, the sensory discharges of their small CS are more delayed and their adaptations to sustained stimuli are less complete (9,11). For CS groups 3 and 6B, the model does not mimic that effect. While the model can be altered to respond similarly to the smaller CS, it was not for this study.

7.8 Limitations

Though my experiments shed light on the role of adaptive load sensing in locomotion, the study is not without limitations. To begin with, the single-leg robotic models do not capture all the dynamics of a free-standing, walking animal. It is well known that the force felt by any one leg can be shaped by the force on other legs (59). Even though I mounted the legs to a carriage that could slide up and down, the rails of the carriage prevented the "bodies" from moving laterally, anteriorly, or posteriorly. The fact that the robotic models are much larger than an insect (15:1, 25:1, 400:1) and that their mass is distributed differently across the legs (i.e., due to dense servos at the end of leg segments) was another limitation of this study. By slowing down the motion of stepping, I was able to compensate for the scale difference and avoid leg strain from vibration such as (Figure 11E). Despite differences in mass distribution, more than 87% of the robot's mass is concentrated in the body because the leg and carriage together weigh 800 g, and less than 100 g can move relative to the carriage. This number is consistent with a locust, whose body makes up 83% of its mass and whose legs comprise 17% of its mass (81,82). Consequently, I anticipate that these findings will be broadly applicable to the animal even though the insects and the robots have different sizes, actuators, and materials.

There were limitations specific to artificial tarsi as well. Insects can grasp objects or the substrate by using an unguitractor mechanism that is affixed to their claws (68). This mechanism of active grip was not implemented due to its complexity. This simplification may not have a major effect on the results because previous biological studies have highlighted the limited function of claws on smooth surfaces such as our treadmill (69). Conversely, because they maintain traction on more uneven surfaces, claws enhance the overall robustness of ground contact (83). This

simplification could be mitigated by reproducing the unguitractor mechanism to incorporate active grip into the robotic model.

In order to directly compare the strain data across various experiments, I also used the same walking kinematics. The nervous system, on the other hand, can adjust stepping kinematics to account for changes in leg structure (losing a leg) or changing terrain. Further work must be done to implement a control program that can modulate the walking kinematics. This control program should utilize the load feedback generated by the CS model to alter its stepping motion in real-time.

8. Conclusion

The aim of this study was to demonstrate the validity of this type of robotic modeling to investigate force encoding, extend the design to include tarsi and compare similar CS morphologies of various insect species by using three dynamically scaled robotic models of the middle leg of the stick insect *C. morosus* and the fly *D. melanogaster*. The difficulty of quantifying such force encoding in an animal, especially one that is free to roam, is the motivation behind these investigations.

By demonstrating that the (15:1) leg can replicate the biological studies carried out on the animal, this goal was achieved. The fact that inertial forces were not dominating the limb further demonstrated that it was, in fact, dynamically scaled adequately. Additionally, disturbances like additional static or transient loading can be encoded by the leg CS. It has also been demonstrated that leg slipping conditions are encoded by the tibia's CS.

Incorporating different tarsus designs that impact load feedback significantly broadened the model. The majority of insects employ tarsi to enhance their ability to locomote, however this is something that is typically avoided when building robots because it complicates construction. Different levels of compliance, passive grip, and biomimetic structure were present in each tarsus design. Every tarsus contributed differently to the strain output, but more study is needed to include active grip in the design.

In the final experiment, the robotic legs of *C. morosus* (25:1) and *D. melanogaster* (400:1) were compared for their morphologically similar CS sites. Stepping kinematics, sensor locations, and leg shape all had a significant impact on the measured stresses. Furthermore, the absence of some sensor locations in one species in contrast to the other encoded strains that the real sensors were already measuring has been demonstrated.

References

1. Pringle JWS. Proprioception In Insects: II. The Action Of The Campaniform Sensilla On The Legs. Journal of Experimental Biology. 1938 Jan 1;15(1):114–31.

2. Spinola SM, Chapman KM. Proprioceptive indentation of the campaniform sensilla of cockroach legs. J Comp Physiol. 1975;96(3):257–72.

3. Zill SN, Chaudhry S, Büschges A, Schmitz J. Directional specificity and encoding of muscle forces and loads by stick insect tibial campaniform sensilla, including receptors with round cuticular caps. Arthropod Struct Dev. 2013 Nov;42(6):455–67.

4. Harris CM, Dinges GF, Haberkorn A, Gebehart C, Büschges A, Zill SN. Gradients in mechanotransduction of force and body weight in insects. Arthropod Structure & Development. 2020 Sep;58:100970.

5. Pearson KG, Iles JF. Nervous Mechanisms Underlying Intersegmental Co-Ordination of Leg Movements During Walking in the Cockroach. Journal of Experimental Biology. 1973 Jun 1;58(3):725–44.

6. Noah JA, Quimby L, Frazier SF, Zill SN. Sensing the effect of body load in legs: responses of tibial campaniform sensilla to forces applied to the thorax in freely standing cockroaches. J Comp Physiol A Neuroethol Sens Neural Behav Physiol. 2004 Mar;190(3):201–15.

7. Keller BR, Duke ER, Amer AS, Zill SN. Tuning posture to body load: decreases in load produce discrete sensory signals in the legs of freely standing cockroaches. J Comp Physiol A. 2007 Aug 1;193(8):881–91.

8. Szczecinski NS, Dallmann CJ, Quinn RD, Zill SN. A computational model of insect campaniform sensilla predicts encoding of forces during walking. Bioinspiration & Biomimetics. 2021 Sep;16(6):065001.

9. Zill SN, Schmitz J, Chaudhry S, Büschges A. Force encoding in stick insect legs delineates a reference frame for motor control. Journal of Neurophysiology. 2012 Sep;108(5):1453–72.

10. Hofmann T, Bässler U. Anatomy and physiology of trochanteral campaniform sensilla in the stick insect, Cuniculina impigra. Physiological Entomology. 1982;7(4):413–26.

11. Zill SN, Büschges A, Schmitz J. Encoding of force increases and decreases by tibial campaniform sensilla in the stick insect, Carausius morosus. J Comp Physiol A. 2011 Aug 1;197(8):851–67.

12. Zyhowski WP, Zill SN, Szczecinski NS. Adaptive load feedback robustly signals force dynamics in robotic model of Carausius morosus stepping. Frontiers in Neurorobotics. 2023;17.

13. Zill S, Schmitz J, Büschges A. Load sensing and control of posture and locomotion. Arthropod Structure & Development. 2004 Jul 1;33(3):273–86.

14. Buschmann T, Ewald A, Twickel A von, Büschges A. Controlling legs for locomotion—insights from robotics and neurobiology. Bioinspiration & Biomimetics. 2015 Jun 29;10(4):041001.

15. Zill SN, Dallmann CJ, S. Szczecinski N, Büschges A, Schmitz J. Evaluation of force feedback in walking using joint torques as "naturalistic" stimuli. Journal of Neurophysiology. 2021 Jul;126(1):227–48.

16. Dallmann CJ, Dürr V, Schmitz J. Joint torques in a freely walking insect reveal distinct functions of leg joints in propulsion and posture control. Proc R Soc B. 2016 Jan 27;283(1823):20151708.

17. Dallmann CJ, Dürr V, Schmitz J. Motor control of an insect leg during level and incline walking. Journal of Experimental Biology. 2019 Apr 1;222(7):jeb188748.

18. Zill SN, Dallmann CJ, Büschges A, Chaudhry S, Schmitz J. Force dynamics and synergist muscle activation in stick insects: the effects of using joint torques as mechanical stimuli. Journal of Neurophysiology. 2018 Oct 1;120(4):1807–23.

19. Harris CM, Szczecinski NS, Büschges A, Zill SN. Sensory signals of unloading in insects are tuned to distinguish leg slipping from load variations in gait: experimental and modeling studies. Journal of Neurophysiology. 2022 Oct;128(4):790–807.

20. Lin DC, McGowan CP, Blum KP, Ting LH. Yank: the time derivative of force is an important biomechanical variable in sensorimotor systems. Journal of Experimental Biology. 2019 Sep 15;222(18):jeb180414.

21. Günzel Y, Schmitz J, Dürr V. Locomotor resilience through load-dependent modulation of muscle co-contraction. Journal of Experimental Biology. 2022 Sep 15;225(18):jeb244361.

22. Grünert U, Gnatzy W. Campaniform sensilla of Calliphora vicina (Insecta, Diptera). Zoomorphology. 1987 Mar 1;106(5):320–8.

23. Delcomyn F. Activity and directional sensitivity of leg campaniform sensilla in a stick insect. Journal of Comparative Physiology A. 1991 Jan;168(1):113–9.

24. Schmitz J. Load-Compensating Reactions in the Proximal Leg Joints of Stick Insects During Standing and Walking. Journal of Experimental Biology. 1993;(183):15–33.

25. Merritt DJ, Murphey RK. Projections of leg proprioceptors within the CNS of the fly Phormia in relation to the generalized insect ganglion. The Journal of Comparative Neurology. 1992 Aug;322(1):16–34.

26. Zill SN, Neff D, Chaudhry S, Exter A, Schmitz J, Büschges A. Effects of force detecting sense organs on muscle synergies are correlated with their response properties. Arthropod Structure & Development. 2017 Jul;46(4):564–78.

27. Dinges GF, Chockley AS, Bockemühl T, Ito K, Blanke A, Büschges A. Location and arrangement of campaniform sensilla in Drosophila melanogaster. Journal of Comparative Neurology. 2021;529(4):905–25.

28. Yasuyama K, Salvaterra PM. Localization of choline acetyltransferase-expressing neurons in Drosophila nervous system. Microscopy Research and Technique. 1999;45(2):65–79.

29. Dinges GF, Bockemühl T, Iacoviello F, Shearing PR, Büschges A, Blanke A. Ultra high-resolution biomechanics suggest that substructures within insect mechanosensors decisively affect their sensitivity. Journal of The Royal Society Interface. 2022;19(190):20220102.

30. Manoonpong P, Patanè L, Xiong X, Brodoline I, Dupeyroux J, Viollet S, et al. Insect-Inspired Robots: Bridging Biological and Artificial Systems. Sensors (Basel). 2021 Nov 16;21(22):7609.

31. Kaliyamoorthy S, Zill SN, Quinn RD, Ritzmann RE, Jongung Choi. Finite element analysis of strains in a Blaberus cockroach leg during climbing. In: Proceedings 2001 Ieee/Rsj International Conference on Intelligent Robots and Systems Expanding the Societal Role of Robotics in the the Next Millennium. IEEE; 2001. p. 833–8.

32. Noda M, Nakamura Y, Adachi K, Saegusa Y, Takahashi M. Dynamic finite element analysis of implants for femoral neck fractures simulating walking. J Orthop Surg (Hong Kong). 2018;26(2):2309499018777899.

33. Wang J, Qian Z, Ren L, Ren L. A dynamic finite element model of human cervical spine with in vivo kinematic validation. Chinese Science Bulletin. 2014 Nov 1;59:4578–88.

34. Wang J, Pang Y, Chang X, Chen W, Zhang J. Mechanical Design and Optimization on Lower Limb Exoskeleton for Rehabilitation. In: 2019 14th IEEE Conference on Industrial Electronics and Applications (ICIEA). 2019. p. 137–42.

35. Khalil HK. Nonlinear systems. 3rd ed. Upper Saddle River, N.J: Prentice Hall; 2002. 750 p.

36. Greenwood DT. Principles of dynamics. 2nd ed. Englewood Cliffs, N.J: Prentice-Hall; 1988. 552 p.

37. Ekeberg Ö, Blümel M, Büschges A. Dynamic simulation of insect walking. Arthropod Structure & Development. 2004 Jul 1;33(3):287–300.

38. Lewinger WA, Rutter BL, Blümel M, Büschges A, Quinn RD. Sensory Coupled Action Switching Modules (SCASM) generate robust, adaptive stepping in legged robots. :11.

39. Lewinger WA, Quinn RD. A hexapod walks over irregular terrain using a controller adapted from an insect's nervous system. In: 2010 IEEE/RSJ International Conference on Intelligent Robots and Systems. 2010. p. 3386–91.

40. von Twickel A, Hild M, Siedel T, Patel V, Pasemann F. Neural control of a modular multi-legged walking machine: Simulation and hardware. Robotics and Autonomous Systems. 2012 Feb 1;60(2):227–41.

41. von Twickel A, Büschges A, Pasemann F. Deriving neural network controllers from neuro-biological data: implementation of a single-leg stick insect controller. Biol Cybern. 2011 Feb;104(1–2):95–119.

42. Dürr V, Arena PP, Cruse H, Dallmann CJ, Drimus A, Hoinville T, et al. Integrative Biomimetics of Autonomous Hexapedal Locomotion. Frontiers in Neurorobotics [Internet]. 2019 [cited 2022 Oct 25];13. Available from: https://www.frontiersin.org/articles/10.3389/fnbot.2019.00088

43. Szczecinski NS, Getsy AP, Martin JP, Ritzmann RE, Quinn RD. Mantisbot is a robotic model of visually guided motion in the praying mantis. Arthropod Structure & Development. 2015 Jul 31;46(5):736–51.

44. Goldsmith CA, Szczecinski NS, Quinn RD. Neurodynamic modeling of the fruit fly Drosophila melanogaster. Bioinspiration & Biomimetics. 2020 Sep;15(6):065003.

45. Cruse H, Bartling Ch. Movement of joint angles in the legs of a walking insect, Carausius morosus. Journal of Insect Physiology. 1995 Sep 1;41(9):761–71.

46. Theunissen LM, Bekemeier HH, Dürr V. Comparative whole-body kinematics of closely related insect species with different body morphology. Journal of Experimental Biology. 2015 Feb 1;218(3):340–52.

47. Dinges GF, Zyhowski WP, Goldsmith CA, Szczecinski NS. Comparison of Proximal Leg Strain in Locomotor Model Organisms Using Robotic Legs. In: Meder F, Hunt A, Margheri L, Mura A, Mazzolai B, editors. Biomimetic and Biohybrid Systems. Cham: Springer Nature Switzerland; 2023. p. 411–27. (Lecture Notes in Computer Science).

48. Composites [Internet]. Markforged; 2022 [cited 2022 Nov 23]. Available from: https://www-objects.markforged.com/craft/materials/CompositesV5.2.pdf

49. Mark Two [Internet]. Markforged; 2022 [cited 2022 Nov 23]. Available from: https://s3.amazonaws.com/mf.product.doc.images/Datasheets/F-PR-2027.pdf

50. Zill SN, Moran DT. The Exoskeleton and Insect Proprioception. I. Responses of Tibial Campanifrom Sensilla to External and Muscle-generated Forces in the American Cockroach, Periplaneta Americana. 1981;26.

51. Delcomyn F, Nelson ME, Cocatre-Zilgien JH. Sense Organs of Insect Legs and the Selection of Sensors for Agile Walking Robots. The International Journal of Robotics Research. 1996 Apr 1;15(2):113–27.

52. Ridgel AL, Frazier FS, Zill SN. Dynamic responses of tibial campaniform sensilla studied by substrate displacement in freely moving cockroaches. J Comp Physiol A. 2001 Jun 1;187(5):405–20.

53. Haberkorn A, Gruhn M, Zill SN, Büschges A. Identification of the origin of force-feedback signals influencing motor neurons of the thoraco-coxal joint in an insect. J Comp Physiol A Neuroethol Sens Neural Behav Physiol. 2019 Apr;205(2):253–70.

54. Zyhowski WP, Zill SN, Szczecinski NS. Load Feedback from a Dynamically Scaled Robotic Model of Carausius Morosus Middle Leg. In: Biomimetic and Biohybrid Systems [Internet]. Springer International Publishing; 2022 [cited 2022 Dec 14]. p. 128–39. (Lecture Notes in Computer Science; vol. 13548). Available from: https://link.springer.com/10.1007/978-3-031-20470-8_14

55. Goldsmith C, Szczecinski N, Quinn R. Drosophibot: A Fruit Fly Inspired Bio-Robot. In: Martinez-Hernandez U, Vouloutsi V, Mura A, Mangan M, Asada M, Prescott TJ, et al., editors. Biomimetic and Biohybrid Systems. Cham: Springer International Publishing; 2019. p. 146–57. (Lecture Notes in Computer Science).

56. Lynch K, Park F. Modern Robotics Mechanics, Planning, and Control. 2017.

57. MATLAB. Natick, Massachusetts: The MathWorks; 2023.

58. Sutton GP, Szczecinski NS, Quinn RD, Chiel HJ. Phase shift between joint rotation and actuation reflects dominant forces and predicts muscle activation patterns. PNAS Nexus. 2023 Oct 1;2(10):pgad298.

59. Dallmann CJ, Hoinville T, Dürr V, Schmitz J. A load-based mechanism for inter-leg coordination in insects. Proceedings of the Royal Society B: Biological Sciences. 2017 Dec 6;284(1868):20171755.

60. Goldsmith CA, Haustein M, Bockemühl T, Büschges A, Szczecinski NS. Analyzing 3D Limb Kinematics of Drosophila Melanogaster for Robotic Platform Development. In: Hunt A, Vouloutsi V, Moses K, Quinn R, Mura A, Prescott T, et al., editors. Biomimetic and Biohybrid Systems. Cham: Springer International Publishing; 2022. p. 111–22. (Lecture Notes in Computer Science).

61. Ridgel AL, Frazier SF, DiCaprio RA, Zill SN. Encoding of forces by cockroach tibial campaniform sensilla: implications in dynamic control of posture and locomotion. J Comp Physiol A. 2000 Apr 1;186(4):359–74.

62. Noah JA, Quimby L, Frazier SF, Zill SN. Force detection in cockroach walking reconsidered: discharges of proximal tibial campaniform sensilla when body load is altered. J Comp Physiol A. 2001 Dec;187(10):769–84.

63. Zill SN, Keller BR, Duke ER. Sensory signals of unloading in one leg follow stance onset in another leg: transfer of load and emergent coordination in cockroach walking. J Neurophysiol. 2009 May;101(5):2297–304.

64. Goldsmith CA, Zyhowski WP, Büschges A, Zill SN, Dinges GF, Szczecinski NS. Effects of Tarsal Morphology on Load Feedback During Stepping of a Robotic Stick Insect Carausius Morosus Limb. In: Biomimetic and Biohybrid Systems. Cham: Springer Nature Switzerland; 2023. p. 442–57. (Lecture Notes in Computer Science).

65. Tajiri R, Misaki K, Yonemura S, Hayashi S. Joint morphology in the insect leg: evolutionary history inferred from Notch loss-of-function phenotypes in Drosophila. Development. 2011 Nov 1;138(21):4621–6.

66. Bennemann M. Biomimicry of the adhesive organs of stick insects (Carausius morosus) [PhD]. RWTH Aachen University;

67. Zill SN, Chaudhry S, Büschges A, Schmitz J. Force feedback reinforces muscle synergies in insect legs. Arthropod Structure & Development. 2015 Nov 1;44(6, Part A):541–53.

68. Gorb SN. Design of insect unguitractor apparatus. J Morphol. 1996 Nov;230(2):219–30.

69. Larsen GS, Frazier SF, Zill SN. The tarso-pretarsal chordotonal organ as an element in cockroach walking. J Comp Physiol A. 1997 May 1;180(6):683–700.

70. Zill SN, Moran DT, Varela FG. The Exoskeleton and Insect Proprioception II. Reflex Effects of Tibial Campaniform Sensilla in the American Cockroach, Periplaneta Americana. 1981;14.

71. Ridgel AL, Frazier SF, Dicaprio RA, Zill SN. Active Signaling of Leg Loading and Unloading in the Cockroach. Journal of Neurophysiology. 1999 Mar 1;81(3):1432–7.

72. Cruse H. What mechanisms coordinate leg movement in walking arthropods? Trends in Neurosciences. 1990 Jan 1;13(1):15–21.

73. Duysens J, Clarac F, Cruse H. Load-regulating mechanisms in gait and posture: comparative aspects. Physiol Rev. 2000 Jan;80(1):83–133.

74. Zill SN, Chaudhry S, Exter A, Büschges A, Schmitz J. Positive force feedback in development of substrate grip in the stick insect tarsus. Arthropod Structure & Development. 2014 Sep 1;43(5):441–55.

75. Dickinson MH. Comparison of Encoding Properties of Campaniform Sensilla on the Fly Wing. Journal of Experimental Biology. 1990 Jul 1;151(1):245–61.

76. Berendes V, Zill SN, Büschges A, Bockemühl T. Speed-dependent interplay between local pattern-generating activity and sensory signals during walking in Drosophila. J Exp Biol. 2016 Dec 1;219(Pt 23):3781–93.

77. Wosnitza A, Bockemühl T, Dübbert M, Scholz H, Büschges A. Inter-leg coordination in the control of walking speed in Drosophila. J Exp Biol. 2013 Feb 1;216(Pt 3):480–91.

78. Szczecinski NS, Brown AE, Bender JA, Quinn RD, Ritzmann RE. A neuromechanical simulation of insect walking and transition to turning of the cockroach Blaberus discoidalis. Biol Cybern. 2014 Feb 1;108(1):1–21.

79. Akay T, Bässler U, Gerharz P, Büschges A. The Role of Sensory Signals From the Insect Coxa-Trochanteral Joint in Controlling Motor Activity of the Femur-Tibia Joint. Journal of Neurophysiology. 2001 Feb;85(2):594–604.

80. Rutter BL, Taylor BK, Bender JA, Blümel M, Lewinger WA, Ritzmann RE, et al. Descending commands to an insect leg controller network cause smooth behavioral transitions. In: 2011 IEEE/RSJ International Conference on Intelligent Robots and Systems. 2011. p. 215–20.

81. Bennet-Clark HC. The energetics of the jump of the locust Schistocerca gregaria. Journal of Experimental Biology. 1975 Aug 1;63(1):53–83.

82. Alexander RMcN. Leg design and jumping technique for humans, other vertebrates and insects. Philosophical Transactions of the Royal Society of London Series B: Biological Sciences. 1995 Feb 28;347(1321):235–48.

83. van Casteren A, Codd JR. Foot morphology and substrate adhesion in the Madagascan hissing cockroach, Gromphadorhina portentosa. Journal of Insect Science. 2010 Jan 1;10(1):40.